THE FLOW AND TEMPERATURE FIELDS IN COOLING DEVICES WITH EMBEDDED SERPENTINE TUBES

Abbreviated title: COOLING DEVICES WITH EMBEDDED SERPENTINE TUBES

I.K. Karathanassis[a, b,*], E. Papanicolaou[a], V. Belessiotis[a] and G.C. Bergeles[b]

[a]Solar & other Energy Systems Laboratory, Institute of Nuclear & Radiological Sciences & Technology, Energy & Safety, National Centre for Scientific Research DEMOKRITOS, Aghia Paraskevi, 15310 Athens, Greece

[b]Laboratory of Innovative Environmental Technologies, School of Mechanical Engineering, National Technical University of Athens, Zografos Campus, 15710 Athens, Greece

[*] Corresponding author: Solar & other Energy Systems Laboratory, Institute of Nuclear & Radiological Sciences & Technology, Energy & Safety, National Centre for Scientific Research DEMOKRITOS, P. O. Box 60228, Aghia Paraskevi, 15310 Athens, Greece. E-mail address: ikarathanassis@ipta.demokritos.gr (I. K. Karathanassis).

The present manuscript has not been published elsewhere and it has not been submitted simultaneously for publication elsewhere.

THE FLOW AND TEMPERATURE FIELDS IN COOLING DEVICES WITH EMBEDDED SERPENTINE TUBES

The turbulent flow (Re=5124) and conjugate heat transfer in heat-sink designs of the tube-on-plate type are numerically investigated. The cooling configurations employ a serpentine tube partially (or fully) embedded inside the plate. A two pass and a four pass configuration are investigated. A constant heat flux is applied at the bottom surface of the heat-sink plate. The SST k-ω model is used for the prediction of the turbulent flow and heat transfer. Two pairs of longitudinal vortices as well as secondary flow separation have been found to set in at the tube curved section. The combined secondary flow pattern enhances heat transfer at the tube sections over a considerable distance downstream of the 180^o bends. In the last part of the analysis, the overall performance of the two configurations is compared using a number of evaluation criteria suitable for heat exchanging devices. The four-pass configuration with fully embedded tubing exhibits the best thermal (energetic) and exergetic performance.

NOMENCLATURE

A	area, m^2
Be	Bejan number $Be = \dot{S}'_{gen,\Delta T} \big/ \dot{S}'_{gen}$
C_p	specific heat, J/kgK
De	Dean number $De = \mathrm{Re}\sqrt{\delta}$
D	tube diameter, m
f	friction factor $f = \Delta p D_i \big/ \left(2\rho L \overline{w}^2\right)$
Gr	Graetz number $\mathrm{Gz} = \dfrac{\pi \,\mathrm{Re}\,\mathrm{Pr}}{2\delta\phi}$
h	heat transfer coefficient $h = \dfrac{-k\left(\partial T \big/ \partial n\right)_w}{\left(T_w - T_{f,m}\right)}$
k	thermal conductivity, W/mK
k	turbulent kinetic energy $k = \frac{1}{2}\left(\overline{(u')^2} + \left(\overline{(v')^2}\right) + \left(\overline{(w')^2}\right)\right)$, m^2/s^2
k*	non-dimensional turbulent kinetic energy $k^* = k \big/ k_{FD}$
L	length, m
$\dot{m}$	mass flow rate, kg/s
Nu	Nusselt number $Nu = \dfrac{h \cdot D_i}{k_f}$
p	pressure, Pa
PI	performance index $PI = \dfrac{\overline{Nu_{ove}}}{f}$
P_{pump}	pumping power, W
q′	heat rate per unit length, W/m
q″	heat flux, W/m^2
R	tube radius, m
R_c	tube radius of curvature, m
Re	Reynolds number $Re = \dfrac{\overline{w} D}{\nu}$
R_{th}	thermal resistance, K/W
s	unwound coordinate, m
S*	non-dimensional unwound coordinate $S^* = \dfrac{s}{D_i}$
$\dot{S}'_{gen}$	entropy generation rate, W/mK
St	Stanton number, $St = \dfrac{Nu}{Re\,Pr}$

T temperature, K

T^* non-dimensional temperature

$$T^* = \frac{T - T_i}{q'' D / k_f}$$

t_s solid substrate thickness, m

u_{tang} non-dimensional velocity projection tangential to the wall (at a local coordinate system)

$$u^*_{\tan g} = \frac{u_{\tan g}}{\overline{w}}$$

$\dot{V}$ volumetric flow rate, m^3/s

W width, m

w flow axial velocity, m/s

w^* non-dimensional axial velocity

$$w^* = \frac{w}{\overline{w}}$$

x,y,z spanwise, vertical and streamwise coordinate respectively, m

X^* non-dimensional spanwise coordinate, $X^* = \frac{x}{D_i}$

Y^* non-dimensional height-wise coordinate, $Y^* = \frac{y}{t_s}$

Z^* non-dimensional streamwise coordinate, $Z^* = \frac{z}{D_i}$

Greek symbols

δ radius ratio, $\delta = \frac{R}{R_c}$

μ dynamic viscosity, Pa·s

μ_t turbulent viscosity, Pa·s

ν kinematic viscosity, m^2/s

ρ density, kg/m^3

τ_w wall shear stress

$$\tau_w = \mu \left. \frac{\partial u_{\tan g}}{\partial y} \right|_{y=0}, \text{ Pa}$$

τ^*_w non-dimensional wall shear stress

$$\tau^*_w = \frac{\tau_w}{\tau_{w,FD}}$$

ω vorticity $\vec{\omega} = \vec{\nabla} \times \vec{\upsilon}$, s^{-1}

ω^* non-dimensional vorticity

$$\omega^* = \omega D / \overline{w}$$

Subscripts

ave	average
cal	caloric
cond	conductive
conv	convective
cs	cross section
f	fluid
FD	value in the fully developed flow region
FE	fully embedded
gen	generation
i	inlet, inner
init	initial
int	interface
max	maximum
o	outer
ove	overall
PE	partially embedded
s	solid, section
tang	tangential
tot	total
w	wall

1. INTRODUCTION

In the field of thermal engineering, curved tubes are incorporated in heat exchanging devices and cooling configurations, as they offer increased heat transfer area per unit volume of the device. In addition, the effect of the centrifugal force on the flow due to the tube curvature induces a characteristic secondary flow, which promotes thermal mixing. Thus, the incorporation of curved tubes into heat exchanging applications can be regarded as a passive heat transfer enhancement technique. The main features of the hydrodynamic and thermal

behavior of fluid flow inside a number of coiled and horizontal curved-tube configurations widely used in industrial processes are summarized in the comprehensive review articles of Vashisth et al. **[1]** and Naphon and Wongwises **[2]**. Apart from the traditional heat exchangers, curved tubes also find application in geothermal heat pumps. Referring to a borehole heat pump, Kobayashi et al. **[3]** numerically investigated the time dependent heat transfer in various serpentine tube configurations embedded in a conductive solid.

Flow in curved tubes has been extensively investigated with the main focus on illustrating the effect of the centrifugal force on the flow field development It has been well established that the secondary flow is manifested through a pair of counter rotating vortices having their axes parallel to the main flow. The prime mechanism responsible for the emergence of the vortex pair is the interaction of the centrifugal force and the induced pressure gradient on the tube cross section **[4,5]**. The experimental investigation of Fairbank and So **[6]** focused on the effect of a 180^o bend on the flow characteristics upstream and downstream straight tube sections. It was demonstrated that the effect of the bend on the axial velocity distribution is more significant in the downstream section, where the velocity profiles appeared distorted for a distance up to seventeen tube diameters. Sugiyama and Hitomi **[7]** used a Reynolds stress model to predict turbulent flow in a tube with an 180^o bend. They presented results regarding the flow field and the secondary flow intensity in the curved as well as the straight downstream section of the tube.

The distinct features of the secondary-flow pattern on the tube cross section are strongly dependent on a similarity parameter known as the Dean number. Different systems of vortical structures may possibly develop depending on the value of the Dean number, as critical values exist that lead to dual solutions for the flow field. Dennis and Ng **[8]** numerically investigated the two-dimensional steady laminar flow in a slightly curved tube. Above a critical value of De=956, they were able to obtain dual solutions that led to either a single or two pairs of symmetrical vortices on cross stream planes. The critical value of the Dean number (De =956) for the onset of a four-vortex structure solution was also confirmed by the numerical study of Yanase et al. **[9]**. Besides, it was stated that the four-vortex system could possibly appear at lower Dean number values, provided that the secondary flow is not fully developed, namely that the secondary flow topology does not remain invariant throughout the entire curved tube. Di Piazza and Ciofalo **[10]** considered the flow in two closed toroidal tubes of different curvature using direct numerical simulation. For Reynolds number values greater than the designated critical ones for each curvature, two distinct traveling waves were detected to emerge in the torus. The first of these affected primarily the Dean vortices, while

the second one manifested itself as an array of oblique vortices in the vicinity of the Dean vortex region. Cheng and Yuen **[11]** performed a flow visualization study in a 180^o bent tube for fully developed laminar flow. Their observations demonstrated that, for Dean numbers equal to 200 and 370, two- or four-vortex systems respectively are possible to emerge, depending on the perturbation of the main flow.

Olson and Snyder **[12]** experimentally proved that the mean axial vorticity in a curved tube initially increases to a maximum value and then decreases asymptotically. They also observed a four-vortex system for De=510 and they adopted the explanation for the onset of the additional vortex pair provided by Rowe **[13]**. In the experimental investigation conducted by Rowe **[13]**, the existence of the additional pair of vortices was attributed to the interaction of the vortex filaments in the vicinity of the inner wall leading to an additional vortex roll-up, which is consequently pushed toward the outer wall by the secondary flow. After reviewing the research that has been conducted regarding the flow in weakly curved tubes, Siggers and Waters **[14]** came to the conclusion that the number of branches of the solution that may be inferred from the findings in the open literature is five. An initial branch of the solution appears even for creeping flows (De<<1), while solution bifurcations leading to dual solutions occur at De=956 and De=2494, respectively. The initial branch is manifested through a two-vortex system, while all other branches through four-vortex systems. However, it must be noted that the critical Dean number values for flow bifurcation reported in theoretical studies are considerably higher than the values for which four vortex systems have been actually observed in experiments **[11,12]**. Besides, according to the theoretical study of Yang and Ye **[15],** a branch of solutions leading to asymmetric recirculation pattern does also exist for Dean numbers exceeding a critical value of 12734.

There is also a number of studies that focus on the heat transfer characteristics for flow inside curved tubes. Mori and Nakayama **[16,17]** theoretically and experimentally investigated heat transfer in a toroidal geometry under uniform heat flux conditions both in the laminar and the turbulent flow regime. They managed to obtain theoretical predictions that correlate the fully developed overall Nusselt number to the Dean and Prandtl numbers. Jayanti et al. **[18]** numerically simulated the flow and heat transfer inside a curved tube of constant pitch (helical coil) by applying a spatially varying centrifugal force on the flow inside a straight tube. Their results illustrate the basic features of the flow and temperature fields under a wide range of heating conditions, both in laminar and turbulent flow.

Kalb and Seader **[19]** conducted a theoretical investigation on the fully developed heat transfer in curved circular tubes under constant heat flux. Their results revealed that the local

Nusselt number at the tube outer wall always obtains larger values than the one at the inner wall and the value of their ratio increases with the Dean number. Besides, the numerical results of Tarbell and Samuels **[20]** referring to Dean numbers of up to 453 showed that the circumferentially averaged local Nusselt number exhibits oscillations as a function of the local Graetz number for moderate Prandtl numbers and under the condition of constant wall temperature. Di Liberto and Ciofalo **[21]** investigated turbulent heat transfer in curved tubes using direct numerical simulation. Through their results, it was established that the temperature fluctuations and the turbulent heat flux obtained maximum values in the vicinity of the outer wall, where secondary flow impingement occurs. In addition, it was illustrated that the enhanced heat transfer observed in curved tubes is not related to turbulence, as the turbulence levels were in fact reduced in comparison to a straight pipe.

Ohadi and Sparrow **[22]** took advantage of the heat and mass transfer analogy and, through the use of the naphthalene sublimation technique, produced experimental values for the Sherwood number characterizing turbulent flow downstream of an 180^o bent. The most interesting finding of the study was that the Sherwood number distribution, for Reynolds numbers having values less than 15000, presented an initial undershoot in the straight tube section downstream of the bent and subsequently redeveloped to a constant value. The authors attributed this heat transfer reduction to flow laminarization occurring at that region. Finally, from the second-law-of-thermodynamics point of view, Bahiraei et al. **[23]** analytically investigated laminar forced convection in a helically coiled tube. They obtained correlations for predicting the Dean number that leads to minimum entropy generation, as a function of the geometrical parameters and heat transfer conditions.

It can be deducted that the majority of the studies dealing with the problem of flow in curved tubes focuses on tubes of constant curvature. On the other hand, the studies concerning U-shaped tubes and especially the effect of an 180^o bend on the flow and heat transfer upstream and downstream of the bend are relatively limited. The scope of the present study is, therefore, to analyze the turbulent flow and conjugate heat transfer inside a tube-on-plate heat-sink design, which incorporates a serpentine tube with 180^o bends (U-turns) thermally bonded to a conductive substrate. Initially, the flow phenomena emerging inside the tubes are identified and thoroughly discussed; then, the effects of the secondary flow and the non-uniform heating conditions on heat transfer are investigated. The heat transfer rate in the straight-tube sections, which are thermally bonded to the substrate, is quantified through distributions of the Nusselt number. The effect of the tubing embedment depth on heat

transfer is also studied. At a final stage, the cooling devices are comparatively evaluated in terms of hydrodynamic and thermal performance.

2. GEOMETRICAL AND OPERATIONAL PARAMETERS

The cooling device under investigation comprises a copper (k_{cu}*=408 W/mK*) serpentine tube thermally bonded to a rectangular aluminum (k_{al}*=237 W/mK*) substrate bearing parallel grooves. The concept of the design is based on a commercially available "cold plate" cooling configurations for thermal management of electronics **[24]**. The present configuration however is intended for application in a linear Concentrating Photovoltaic/Thermal (CPVT) system designed by the authors **[25],** in order to extract the surplus heat from a solar-cell module. The overall area of the substrate is 500 x 60 mm^2 corresponding to the receiver area of the CPVT system.

The serpentine tubing forces the coolant flowing inside to divert its course by 180^o, in order to pass multiple times through the solid substrate. It must be noted that the straight parts of the tube are partially embedded in the substrate, whereas the curved bends lay outside of the plate area, as depicted in **Figure 1**. Two variations of the heat-sink design are addressed in the present analysis having two (**Figure 1a**) and four (**Figure 1b**) equidistant straight tube segments on the substrate respectively.

The operating conditions for the cooling device are determined by taking into account the specifications of the other components comprising the CPVT system and typical environmental conditions. For a concentrator-reflector area equal to 1 m^2 and typical one-sun irradiation (1 kW/m^2), the irradiation on the receiver area results to 33.3 kW/m^2. 15% of the irradiation is directly converted to electricity by the solar-cell module, while the remaining (28.3 kW/m^2) is to be dissipated by the heat sink. Water is selected as cooling fluid with a fixed volumetric flow rate equal to 30 ml/s, which is adequate for hot water for domestic use.

3. FORMULATION OF THE NUMERICAL MODEL

3.1 Governing equations

The computational domain consists of two solid and one fluid sub-domains corresponding to the substrate, the tubing and the cooling fluid, respectively. The thermophysical properties

of the coolant are considered constant and evaluated at 298K. The problem under investigation allows the following assumptions to be made:

(1) steady, turbulent and incompressible fluid flow (Re=5124)

(2) negligible viscous dissipation and radiative heat transfer

(3) negligible natural convective heat transfer, since the parameter Gr/Re^2 takes values much smaller than unity.

Based on these assumptions, the three-dimensional transport equations of mass, momentum and energy reduce to the following form:

(continuity) $$\frac{\partial}{\partial x_i}\left(\rho\bar{u}_i\right)=0 \tag{1a}$$

(momentum) $$\rho\frac{\partial}{\partial x_j}\left(\bar{u}_i\bar{u}_j\right)=-\frac{\partial\bar{p}}{\partial x_i}+\frac{\partial}{\partial x_j}\left[\mu\left(\frac{\partial\bar{u}_i}{\partial x_j}+\frac{\partial\bar{u}_j}{\partial x_i}\right)-\rho\overline{u_i'u_j'}\right] \tag{1b}$$

(energy) $$\rho C_p\frac{\partial}{\partial x_i}\left(\bar{u}_i\bar{T}\right)=\frac{\partial}{\partial x_i}\left[k\frac{\partial\bar{T}}{\partial x_i}-\rho C_p\overline{u_i'T'}\right] \tag{1c}$$

The Reynolds Averaged Navier-Stokes (RANS) equations formulated above contain the Reynolds stresses terms $\overline{u_i'u_j'}$ and the turbulent heat flux $\overline{u_i'T'}$. The Shear Stress Transport (SST) k-ω model introduced by Menter **[26]** is used for the calculation of these terms. The SST model uses appropriate blending functions in order to switch between the k-ω and the k-ε model formulations depending on the distance from the wall; therefore the k-ω formulation is used in the near-wall region in order to avoid the use of any extra damping functions, while the k-ε formulation is used in the fluid-core region. The additional equations introduced for the turbulent kinetic energy *k* and the turbulent frequency *ω*, as well as all the additional relations and coefficients used by the model are listed in **[27]**.

By taking into consideration the actual operating conditions of the cooling device, appropriate boundary conditions are imposed on the governing equations. The imposed boundary conditions are summarized in **Table 1.** The momentum and energy equations are fully coupled and solved simultaneously on an unstructured hexahedral grid using the commercial solver ANSYS CFX (v.13) **[27]**. The convergence criterion for the RMS (root mean square) residuals of mass, momentum and energy is set equal to 10^{-6}. False transient time stepping is used in order to control convergence and an appropriate time step equal to 25% of the fluid residence time $t=L/\bar{w}$ inside the tubing is selected.

3.2 Grid independence

The computational domains for both cooling configurations were discretized using unstructured grids of hexahedral elements (**Figure 2**). The grids had a non-uniform arrangement along the flow direction, as a fine grid was used along the curved sections of the domain (**Figure 2a**), in order to fully capture the topology of the expected secondary flow. In addition, the grid nodes were closely positioned in the fluid cross section adjacent to the solid wall (**Figure 2b**), in order to capture the steep gradients in the boundary layer region. A grid independence study was conducted in order to verify that the produced computational results remained unaffected from the grid density. For this reason, the four-pass configuration was selected and simulations were performed using three grids of increasing density, namely of 1.2, 2.6 and 4.0 x 10^6 elements, respectively.

The coolant pressure drop through the configuration, the substrate maximum temperature and the overall Nusselt number were considered as adequate quantities in order to ensure the grid independency of the solution. As it is evident from the values of **Table 2**, the computational grid consisting of 2.6 x 10^6 elements is suitable for the production of the numerical results, as a further grid refinement to 4.0 x 10^6 elements causes all the monitored quantities to deviate by less than 1%. Subsequently, the computational domain for the two-pass configuration was discretized using elements of the same dimensions and topology, as those comprising the selected grid for the four-pass configuration, and the final grid consisted of $2.2 \cdot 10^6$ elements.

3.3 Validation of the numerical model

In order to verify that the formulated numerical model can adequately predict the effect of the centrifugal force on a curved-tube flow, numerical results were produced and compared against published data regarding flow in curved pipes **[5,6]**. Patankar et al. **[5]** predicted the turbulent flow in a curved tube having a δ ($=R/R_c$) ratio equal to 0.025 using the standard k-ε turbulence model. The horizontal and vertical fully developed velocity profiles published in **[6]** for Reynolds number equal to 25000 are compared with the respective ones calculated in the present study using the SST k-ω model (**Figure 3a**). As can be seen, the predictions of the two models are in good agreement and the velocity overshoots are captured in both planes.

Fairbank and So **[6]** obtained experimental velocity profiles at the horizontal symmetry plane of two U-shaped tubes characterized by different δ ratios equal to 0.08 and 0.30, respectively. The Reynolds number was maintained the same in both cases and equal to 400, while the Dean number was equal to 110 and 220, respectively. The comparison between the present numerical results, which were produced using a computational domain similar to the experimental setup described in **[6]**, and the experimental data is shown **Figures 3b-e,** where the velocity profiles at two dimensionless positions *s/2a* downstream of the bend and equal to 0.5 and 5.0 are compared. Good agreement is evident with the root mean square deviation not exceeding 3%, with the uncertainty in the experimental velocity values being 2.5%. The shift of the maximum velocity toward the outer wall is also well captured.

4. RESULTS AND DISCUSSION

4.1 Flow Field

The flow inside the tubing of both configurations is characterized by the same Reynolds number equal to 5124. However, the value of the Dean number varies due to the different ratio of the tube radius to the bend curvature radius δ, giving the Dean numbers of 2763 and 3867 for the two-pass and four-pass configurations respectively. **Figures 4a-b** present non-dimensional axial velocity profiles at the horizontal symmetry plane of the tube for several streamwise positions downstream of the bend. Especially regarding the four-pass configuration (**Figure 4b**), the streamwise positions refer to the straight tube section downstream of the first bend encountered by the flow. As can be seen, the velocity profile appears distorted downstream of the bend for both configurations; the maximum velocity location is shifted toward the outer wall, with the maximum velocity being higher for the higher Dean number configuration (four-pass configuration). However, the velocity profiles at Z^*=58.53 and Z^*=56.53 for the four-pass configuration exhibit off the wall minimum velocity and thus a second peak of the velocity value in the vicinity of the inner wall, a feature not present in the two-pass configuration. The velocity minimum and thus the second velocity peak near the inner wall for the four-pass configuration is due to a strong recirculation zone which develops (as the result of the higher Dean number) and draws high-velocity fluid from the tube core toward the inner wall. In addition, the velocity profiles at Z^*=28.53, a location slightly downstream of the straight-section mid-length, appear almost

fully developed and therefore it is obvious that the flow is recovering to a development state in the straight section of the tubes. Thus, with regard to the four-pass configuration, the flow upstream of each bend develops fully after the previous bend and identical flow phenomena repeat themselves in each curved section and downstream of it.

Figures 4c-d illustrate the developing flow field within the bends of the two-pass (**Figure 4c**) and four-pass (**Figure 4d**) configurations through streamlines. It must be noted that streamlines have been drawn only for the upper half of the tube cross-section as the flow field is symmetric about the horizontal plane. Two bundles of streamlines, highlighted with different colors, have been drawn in order to elucidate the topology of the secondary flow that sets in at the curved region. Black lines originating near the central part of the duct develop an extensive whirling effect that occupies the entire tube half cross section and is associated with the Dean vortices as will be discussed later, whereas in the case of streamlines from the outer part of the cross section (red lines) this effect is more localized in the vicinity of the inner wall. Regarding the four-pass configuration (**Figure 4d**), a recirculation bubble due to axial flow separation is also visible. The secondary flow pattern will be further analyzed in the following paragraphs.

Figure 5 depicts the distribution of the non-dimensional wall shear stress at the intersections of the horizontal symmetry plane with the tube wall as a function of the non-dimensional "unwound" coordinate S^*, in the sense that the *s* coordinate follows the curved section of the tube as well as the upstream and downstream straight ones. Consequently, the S^* coordinate obtains a slightly larger value for the outer wall due to the larger radius of curvature of the outer curved section. Regarding the four pass configuration, it must be noted that the wall shear stress values are plotted only for the two first passages, as the same behavior is expected to be repeated in the following two. Upstream of the bend, after an initial adjustment due to the uniform inlet velocity, the shear stress value remains constant and identical for the inner and outer walls in both configurations. In the curved section, the two walls are differentiated as the shear stress exhibits more rapid changes at the inner wall for both configurations (**Figures 5a-b**). A sign change of the shear stress values sign is observed at the distribution of the inner wall in both graphs, a clear indication of flow separation. It is interesting to notice that flow separation also occurs at the outer wall of the four-pass configuration (**Figure 5b**); however, it is of negligible magnitude and the shear stress regains positive values almost immediately. Indeed, as depicted on the inset of each graph a recirculation bubble exists on the horizontal (XZ) plane in the vicinity of the inner wall for both configurations. The insets depict contours of the tangential to the wall velocity

in a local coordinate system, so that negative values indicate flow recirculation. The recirculation bubble is located at the downstream straight section in the two-pass design (**Figure 5a**), whereas a close look at the contours regarding the four-pass design (**Figure 5b**) reveals that, in fact, two connected bubbles exist having their centers at the straight section downstream of the curve and in the vicinity of the inner curve apex respectively. Besides, it is interesting to notice that the shear stress distributions of the inner and the outer wall in the straight section downstream of the bend are not identical, as in the upstream section. Although, the inner-wall distribution of the four-pass configuration exhibits a local minimum approximately at S^*=71, the two lines coincide to a common value further downstream.

Figure 6 illustrates clearly the sequence of the creation of the vortical structures that set in in the curved section of the tube through vorticity projection plots at several cross-stream planes along the curved as well as the downstream straight tube section. At $\varphi=60^o$, a pair of Dean vortices having their centers shifted toward the inner wall is already evident in both configurations (**Figures 6a-b**). The vortices have opposite vorticity sign with regard to the wall vorticity at the respective locations. In fact, the vertical distance between these locations of concentrated wall vorticity appears to be smaller in the four-pass configuration. In addition, a second pair of vortices can be clearly seen at $\varphi=90^o$ for the two-pass configuration (**Figure 6a**) but less developed for the four pass configuration which however is clearly seen at $\varphi=120^o$ (**Figure 6b**). It seems that the development of the secondary flow pattern is affected by the Dean number and the additional vortices emerge further downstream along the bend arc as the Dean number increases. This second pair of vortices is initially more localized in the vicinity of the Dean vortices, but as the flow travels further downstream in the bend (e.g. see plots at $\varphi=150^o$), the vortices become oblique and elongated (kidney shape) with their upper part moving toward the tube center. These "middle" vortices interact with the Dean vortices and significantly distort their topology in both configurations. The onset of the middle vortices due to the localized vorticity created by the mutual approach of the symmetrical Dean-vortex filaments that leads to an additional vortex roll-up and the subsequent drifting of the vortex-pair toward the tube core observed in the present investigation is in agreement with the findings of Rowe **[13]** who reports that the additional pair of vortices emanates at the boundaries of the Dean vortices and is then pushed toward the outer wall by the secondary flow. Another region of high vorticity can be detected near the inner tube wall in both configurations due to the secondary flow separation. This "inner" vortex pair gradually increases in size as φ increases. Additional discussion on the secondary flow topology under different flow conditions is provided in paragraph 4.2. The vortex

system persists in the downstream straight section, gradually reducing in magnitude and the additional pair of vortices decays completely at approximately a distance of eight hydraulic diameters downstream of the bend (Z^*=52.53). **Figure 6c** depicts the distribution of the average of the non-dimensional streamwise vorticity magnitude in the curved section. It can be seen that higher values are obtained in the four-pass configuration due to the higher Dean number; regarding the two-pass configuration, the peak vorticity value is obtained at $\varphi=90^o$ and the distribution is approximately symmetrical about the center of curvature. On the contrary, the distribution is strongly asymmetrical in the four-pass configuration with a peak value at $\varphi=135^o$.

Figure 7 presents contours of the non-dimensional turbulent kinetic energy k^* in the curved and the downstream sections of the two configurations. Regarding the curved section, the contour lines already appear distorted in the region close to the tube inner part at $\varphi=60^o$. The distortion becomes more intense as the flow travels through the curved section. For the two-pass configuration (lower Dean number) turbulence levels increase up to 120^o to 150^o in the bent and then start decreasing, whilst in the four-pass configuration turbulence keeps increasing up to the exit of the bend; the maximum turbulence level attained is approximately three times higher compared to that for the two-pass configuration. Turbulence maxima along the bend are found near the inner part of the bend and in proximity to the centers of the vortices on the cross stream planes. As depicted in **Figures 7a-b,** the turbulent kinetic energy values in the downstream section of both configurations appear significantly reduced in comparison to the ones in the respective curved sections. The profiles gradually redevelop to a fully developed, symmetrical form (Z^*=2.53) and the mean turbulent kinetic energy in the tube cross-section obtains the expected value equal to that in the upstream section. It is of interest also to notice that the location of the maximum k^* is at different positions for the two configurations; for the two-pass configuration the k^* maximum is near the wall, whilst in the four-pass configuration the corresponding maximum is near the center of the tube. This can be explained by the fact that in the four-pass configuration the locations from which the vortices appear to be shed are closer to the central plane and this coupled with the much stronger secondary flow due to higher Dean number transports the wall-generated turbulence towards the center plane. A close look at **Figure 7b** reveals that, in the four-pass configuration, the turbulent kinetic energy obtains a minimum value at Z^*=44.53 and subsequently increases again. Further insight into this distinct behavior can be gained through **Figure 7c,** which presents values of the averaged over the cross section non-dimensional turbulent kinetic energy as a function of the "unwound" coordinate S^*. It is clear

that the turbulent kinetic energy initially increases rapidly in the curved section of both configurations and then drops in the subsequent straight section. The peak value is attained within the curved section, at approximately $\varphi=120^{o}$, in the two-pass configuration and slightly downstream of it, approximately half a hydraulic diameter, in the four-pass configuration. The distribution subsequently exhibits a steep decreasing trend and minimum values are obtained at $S^{*}=13$ for the two-pass and $S^{*}=17$ for the four-pass configuration, respectively. This significant reduction of the turbulent kinetic energy in the straight section downstream of the bend is indicative of a flow tendency to transition to the laminar regime and it is attributed to the fact that the axial velocity profiles at downstream locations with Z^{*} less than 52.53 tend to obtain a flat form with lower velocity gradients than the fully developed profile, e.g. see the axial velocity profile at Z*=52.53 of **Figure 4b**. This is a remaining consequence of the secondary flow which considerably distorts the form of the upstream fully turbulent velocity profile.

4.2 Effect of the Reynolds number - parametric analysis

The flow field in the curved tubes is significantly affected by the flow conditions and the tube geometry and thus different vortical structures are possible to arise. Yanase et al. **[28]** proposed that, regarding tubes of finite curvature, the effect of the Reynolds number and δ should be treated as independent factors, as the appearance of additional vortices could be attributed to either the flow convective effect or the centrifugal effect due to curvature. So et al. **[29]** investigated laminar flow in U-shaped tubes of small curvature and identified the Reynolds number, the δ ratio and the flow profile at the entrance of the bend as the three main factors that determine the characteristics of the emerging secondary flow pattern. It was concluded that an additional pair of vortices symmetrical about the horizontal plane always emerges in the tube center under the condition that the velocity profile at the entrance of the bend is fully developed.

In order to further elucidate the topology of the vortex system that emerges under different flow conditions in the cooling configurations investigated, a parametric analysis has been carried out for lower values of the Reynolds number, covering a wide range within the laminar flow region (Re=100-1600). The two-pass configuration has been selected for the parametric analysis, as it is more favorable in terms of computational cost in comparison to the respective four-pass configuration. **Figure 8** presents the cross-stream secondary flow patterns in the form of vorticity contour plots and normalized vector plots at a sample plane

midway along the bend ($\varphi=90^o$). For Reynolds number equal to 100, only a pair of symmetrical Dean vortices can be detected having their centers lying almost at the vertical symmetry plane of the tube cross-section. As the Reynolds increases to 200, the vortices become skewed and their centers shift toward the tube inner wall, however, still a two-vortex solution is evident. On the contrary two distinct pairs of vortices are clearly discernible in the Reynolds number range 400-1600, with the second pair of oblique vortices located approximately at the tube center. Yanase et al **[28]** reported that for $\delta=0.29$ as in the present case, the onset of the additional pair of vortices is possible at Reynolds number values higher than 270. An additional feature that can be observed is the secondary flow separation near the inner wall, which gains in coherence as the Reynolds number increases, and is clearly manifested at Re=1600 in the form of a pair of localized vortices attached to inner wall and in the vicinity of the horizontal symmetry plane. The resulting "three cell topology" is in agreement with the findings of So et al. **[29]** and also with the experimental observations of Agrawal et al. **[30]** and Choi et al. **[31].** The distinct vortical structures detected in the laminar flow region clearly persist in the turbulent region as well, as revealed by comparing **Figures 6a-b** and **8**.

Figures 9a-b give a perception of the magnitude increase of the vortical structures with Re. As depicted in **Figure 9a**, the location of the maximum average non-dimensional vorticity magnitude at the tube cross-section slightly shifts toward the bend middle ($\varphi=90^o$) as the Reynolds number increases. In all cases, the maximum averaged vorticity value has been obtained by $\varphi=75^o$ and a decreasing trend is clearly followed after $\varphi=90^o$. By comparing **Figure 9a** to **Figure 6c**, it can be seen that higher values of the non-dimensional vorticity are obtained in the laminar flow region, thus the $\overline{\omega}/\overline{w}$ ratio decreases as the Reynolds number increases. This is an indication that the magnitude of the secondary flow pattern increases at a lower rate with Re in the turbulent flow region. **Figure 9b** shows the maximum vorticity magnitude of the Dean and middle vortices at the sample plane at $\varphi=90^o$ as a function of the Reynolds number. As illustrated, the relative increase in the magnitude of the Dean vortices is smaller as the Reynolds number increases, a trend which confirms the remark made regarding the vorticity magnitude in the turbulent flow region. The magnitude of the middle vortices, on the other hand, increases in a nearly linear manner with the Reynolds number. However, the maximum magnitude attained by the middle vortices (at Re=1600) is approximately half the respective one of the Dean vortices.

Finally, two further simulations have been conducted in the turbulent flow regime (Re=10248 and 20496 leading to De=5527 and 11053 respectively) in order to illustrate the flow tendency to re-transition to the laminar regime in the straight tube section adjacent to the bend (see **Figure 7**). **Figure 10** presents the distribution of the average turbulent kinetic energy with the Reynolds number as parameter. It can be observed that an increase of the Reynolds number shifts the undershoot of the turbulent kinetic energy to lower values and, in addition, towards axial positions further downstream of the bend. It is evident by comparing **Figures 7c** and **10** that, although the Dean number for the four-pass configuration is lower (De=3867), the higher value of δ in comparison to the two-pass configuration has a similar effect in the turbulent kinetic energy distribution, as for the case of Re=10248 in **Figure 10**. Thus, it can be concluded that the Reynolds number and δ affect the turbulent kinetic energy distribution in an independent manner and thus should be rather treated as distinct parameters instead of combining their effect in the Dean number.

4.3 The temperature field

As shown in **Figure 11a** through contour plots of the non-dimensional temperature, the flow reaches full thermal development in the straight tube section upstream of the bend. It is interesting to notice that the thermal boundary layer in the lower part of the tube is thicker in comparison to the upper one. This is due to the non-uniform heating conditions, as the tube is mainly heated through the part of its circumference that is embedded in the substrate, which is approximately equal to three quarters of the total. The flow behavior upstream of the bend is identical for the two- and four-pass configurations and **Figure 11a** indicatively contains results only for the two-pass configuration.

The effects of the secondary-flow pattern are significant in the development of the temperature field downstream of the bend as intense thermal mixing takes place in both configurations (**Figures 11b-c**). Cold fluid is deflected toward the outer tube wall causing the disruption of the boundary layer development in that region. On the contrary, the maximum fluid temperature values are detected in the inner tube wall and especially in the vicinity of the horizontal symmetry plane, where the thermal boundary layer is also locally thickened. This is due to the secondary flow, which, after impinging on the outer wall, is symmetrically diverted toward the lower and upper part of the tube circumference, where it draws fluid from the boundary layer region and guides it to the symmetry plane of the inner wall. The effect of the secondary flow gradually weakens in the straight section and the flow redevelops. As can

be seen from the contour plot at Z^*=28.53, the fully developed profile is slightly distorted toward the outer wall. It must be noted that **Figure 11c** refers to the second pass of the four-pass configuration. The temperature distribution in the respective regions of the other downstream passages is qualitatively identical. However, the absolute temperature values are higher as the fluid is constantly heated throughout the substrate area (**Figure 11d**).

It is also of importance to illustrate the temperature distribution in the solid substrate as this is indicative of the thermal performance of the cooling device. As shown in **Figure 12,** the temperature field is fully three-dimensional in both configurations due to the effect of axial conduction, enabled by the high thermal conductivity of the substrate material. It is clearly discernible that the substrate region of high temperatures is shifted in both configurations toward the section of the heat-sink close to the tubing outlet, with the maximum temperature located at the left vertical wall approximately ten hydraulic diameters upstream of the outlet; the maximum wall temperature is higher for the two-pass configuration (**Figure 12a**) due to the smaller area available for heat transfer between the substrate and the tubing. Besides, it is evident that the transversal temperature distribution of the substrate is primarily influenced by the fluid temperature inside the tubing, which is embedded by approximately three quarters of its circumference. Thus, the region of the heat sink closer to the inlet passage obtains lower temperatures. In fact, the effect of the fluid temperature on the substrate is manifested in a more regular manner in the four-pass configuration **(Figure 12b)**.

4.4 Effect of the tube embedment

The relative position of the tube center to the heated surface (Y^*=0) is a manufacturing parameter that can significantly differentiate the temperature field in the heat sink and is expected to have a significant effect on its thermal performance. In order to elucidate the effect of the tube embedment into the substrate, two additional variations of the cooling configuration have been examined, similar to the two-pass and four-pass configurations of **Figure 1**, with the difference that the center of the tubing cross section is located exactly at the middle of the substrate (Y^*=0.5). **Figure 13** depicts the vertical non-dimensional temperature profiles at two and four characteristic span-wise (X^*) locations, respectively, along the heat sink streamwise mid-length (Z^*=30.25), in order to illustrate the temperature distribution in both the solid and the fluid regions of the heat sink. Heat is distributed through conduction in the lower and upper solid parts of the cooling device and through convection in

the fluid section inside the tubing. Regarding the fluid region, it can be seen that the temperature profiles remain invariant regardless of the tubing position and, regarding the four-pass configuration, the fluid is being heated at a higher rate in the two passages (X^*=2.63 and X^*=0.88) closer to tube inlet, as revealed by the temperature difference between consecutive profiles in **Figure 13b**.

The discernible linear parts of the profiles clearly show that the substrate temperature also increases in the design employing fully embedded (FE) tubes, as the outer vertical side closer to the outlet is approached, i.e. the X^* coordinate decreases. Furthermore, it is evident that the fully embedded tubing leads to reduced temperature at the lower part of the substrate and consequently at the heated bottom side (Y^*=0) as well, which is an indication of enhanced thermal performance. The transversal temperature distribution at the substrate, which is not presented for brevity, has a similar form to the designs employing partially embedded tubes (see **Figure 13**). Nonetheless, the absolute temperature values are decreased in the configurations employing fully embedded tubes.

4.5 Local Nusselt number distribution

The quantification of the heat transfer rate is limited to the straight sections of the serpentine tube, as the curved sections lay outside of the substrate active area. The local Nusselt number values presented are based on the averaged -over the tube circumference- values of the convective heat transfer coefficient at each streamwise location z:

$$\bar{h}(z) = \frac{\bar{q}(z)}{\overline{T_w}(z) - \overline{T_f}(z)} \tag{2}$$

In the above expression, $\bar{q}(z)$ and $\overline{T_w}$ are the circumferentially averaged heat flux and tube wall temperature values, respectively, whereas $\overline{T_f}(z)$ is the local fluid bulk mean (mixing cup) temperature defined as:

$$\overline{T_f} = \frac{1}{\bar{w} A_{cs}} \int_{A_{cs}} w(x,y) T(x,y) dA_{cs} \tag{3}$$

with $\bar{w}$ the mean flow velocity inside the tube and A_{cs} the tube cross sectional area.

Figure 14 presents the local Nusselt number distribution in the straight sections of the cooling configurations considered. For the longest portion of the straight sections in both

configurations, the Nusselt number exhibits constant, fully developed values. The fully developed value is slightly different in each passage, a behavior that should be attributed to the non-uniform heating, as the temperature distribution in the substrate is fully three dimensional. Furthermore, the designs employing fully embedded tubes attain higher Nusselt number values, by as much as 5% in the four-pass configuration. The temperature non-uniformity is higher in the substrate of the designs with fully embedded tubes and non-uniform heating conditions have been reported to enhance heat transfer **[32]**.

Figure 14 also reveals that the Nusselt number distribution in the first passage of both configurations exhibits a minimum point right after the thermal entrance region and subsequently redevelops to a fully developed value. This behavior is in contrast to the monotonically decreasing one typically encountered in tubes subject to a constant wall temperature or heat flux and is due to the conjugate effects. The reduced heat transfer in the early section is explained by taking into consideration the low substrate temperature in the specific region (see also **Figure 12**), which leads to a decreased temperature gradient. The local Nusselt number obtains high values in the tube section immediately downstream of the bend and more specifically at the range Z^*=50-60 in the two-pass (**Figure 14a**) and Z^*=45-60 in the four-pass configuration (**Figure 14b**), respectively. This heat transfer enhancement (by nearly a factor of 1.5) is due to the effect of the secondary flow, which constantly feeds the circumferential boundary layer area with colder fluid from the tube core. It is justifiable, that the high heat-transfer region has a greater extent in the four-pass configuration due to the higher intensity of the recirculation (also see **Figure 6**). It is also interesting to note that in the region Z*=30-50 in **Fig. 14a** the values for the first and second pass almost overlap and exhibit a flat distribution, for both the FE and PE cases, indicative of a thermally fully-developed region, unaffected from any end or curvature effects. A close look at **Figures 14a-c** also reveals that the local Nusselt number distribution exhibits an undershoot in the subsequent tube section, where the longitudinal vortices have decayed completely. The region in question extends approximately to the streamwise distance Z^*=40-50 in the two-pass configuration and Z^*=35-45 in the four-pass configuration, respectively. A similar undershoot has also been observed by Ohadi and Sparrow **[22]** who attributed it to flow re-transition to the laminar regime. The findings of the present study support their assumption, as can be established by comparing **Figures 7c** and **14**. It is evident that the turbulent kinetic energy values are considerably reduced in the region of the Nusselt number undershoot.

4.6 Comparative analysis

A number of criteria have been selected in order to elucidate each aspect of the heat-sink performance. A suitable measure for the quantification of the thermal performance of a cooling device is the thermal resistance. The overall thermal resistance is determined on the basis of an equivalent resistance circuit:

$$R_{tot} = R_{cond} + R_{cal} + R_{conv} = \frac{t_s}{k_s A} + \frac{1}{\rho \dot{V}_{tot} c_p} + = = \frac{1}{\overline{h_{ove}} A_{HTR}} \tag{4}$$

where the three terms on the right hand side of **Eq. (4)** correspond to the conductive, caloric and convective individual resistances. In addition, the temperature non-uniformity at the heated surface ($Y^*=0$) is estimated through the standard deviation of temperature. Hydrodynamic performance can be adequately represented through the required pumping power $P_{pump} = \dot{V} \cdot \Delta p$ which, for a constant flow rate, is determined by the pressure drop values. Besides, an indication of the overall performance of a heat exchanging device is the heat transfer to pressure drop ratio **[34]**. In the present study, this overall performance index is calculated in a non-dimensional form as $PI = \frac{\overline{Nu_{ove}}}{f}$, where $\overline{Nu_{ove}}$ is the overall mean Nusselt number and *f* is the friction factor calculated through $f = \Delta p D_i / \left(2 \rho L \overline{w}^2\right)$.

From the point of view of the second-law of thermodynamics, the cooling devices can be evaluated through the concept of the entropy generation rate, which is equivalent to the destruction of available work. The entropy generation rate per unit length of a duct having an arbitrary cross-section can be calculated using averaged quantities regarding heat transfer and fluid friction **[35]**:

$$\dot{S}'_{gen} = \frac{q'^2}{4 \overline{T}_f^2 \dot{m} c_p} \frac{D}{\overline{St}} + \frac{2 \dot{m}^3}{\rho^2 \overline{T}_f} \frac{f}{D A_{cs}^2} \tag{5}$$

where q' is the heat rate per unit length and $\overline{St}$ is the mean overall Stanton number. The two terms on the right hand side of **Eq. (5)** correspond to the contribution of heat transfer and friction losses, respectively, to the entropy generation rate. The discrete contribution of each

term to the total entropy generation rate can be designated through the Bejan number $Be = \dot{S}'_{gen,\Delta T} \Big/ \dot{S}'_{gen}$.

The comparative results of the considered cooling configurations with regard to the above mentioned criteria are summarized in **Table 3**.The two-pass configuration is superior in terms of hydrodynamic performance, as the length of the employed serpentine tube is less than half in comparison to the four-pass. Besides, the existence of two additional recirculation regions in the four-pass configuration also induces further pressure losses. In addition, the two-pass configurations exhibit higher temperature uniformity in the substrate bottom surface. As less substrate area is occupied by tubes in comparison to the four-pass designs, the effect of the conductive substrate which tends to homogenize the temperature distribution is more significant leading thus to greater uniformity. It must also be noted that full embedment of the tubing deteriorates temperature uniformity in both configurations. However, the four-pass configurations exhibit much smaller values of the thermal resistance, which is a far more critical parameter for the heat-sink performance in comparison to temperature non-uniformity. Especially, the design employing fully embedded tubes achieves the minimum value, as it offers the largest area available for heat transfer in comparison to the other configurations. The values of the performance index are within 5% for all the considered configurations and do not seem appropriate in the specific case for drawing a meaningful conclusion

Regarding the exergetic performance, the four-pass configurations achieve much lower values of the entropy generation rate primarily due to the distribution of the same heat rate to four, instead of two, straight tube sections (see **Eq. 5**). The four-pass configuration with fully embedded tubes obtains the lowest value of the entropy generation rate, also due to the higher value of the overall Nusselt number it achieves. Besides, the values of the Bejan number illustrate the fact that the values of the total entropy generation rate are primarily determined by the first term on the right hand side of **Eq. 5** corresponding to heat transfer. It must be noted that the effect of the secondary flow in **Eq. 5** is included in the Stanton number and the friction factor *f* regarding the heat-transfer and the friction-loss terms, respectively.

5. CONCLUSIONS

The turbulent flow and conjugate heat transfer in two tube-on-plate cooling devices was investigated by means of a three dimensional numerical model. A two-pass and a four-pass configuration were investigated with flow conditions characterized by Dean numbers equal to 2763 and 3867 respectively. It was found that a pair of localized vortices close to the inner wall, a pair of Dean vortices and a pair of oblique vortices at the tube center emerge within the bends of both configurations and persist in the adjacent downstream, straight-tube sections. The same vortex structures were also visible over a wide range of Reynolds numbers after extending the investigation into the laminar flow regime (Re=400-1600). In addition, a rapid decrease of the turbulent kinetic energy indicating a flow tendency to re-transition to the laminar flow regime was detected in the straight tube section downstream of the bend. Besides, it was established that an increase in the Reynolds number and/or δ have an independent effect on the downstream turbulent kinetic energy distribution and tend to lower the value of the minimum turbulent kinetic energy point.

In the substrate area, it was found that the maximum temperature occurs at the side vertical wall close to the tube outlet in both configurations. It was furthermore proved that full embedment of the tubing into the substrate reduces the substrate temperature. The local Nusselt number distributions demonstrated that the heat transfer rate is significantly enhanced in the regions subject to the influence of the longitudinal vortices, followed by an undershoot in the regions adjacent to them due to reduction in turbulent kinetic energy.

The comparative evaluation showed that the two-pass configurations were superior in terms of hydrodynamic performance and temperature uniformity. On the other hand the four-pass configurations obtained much lower values of the thermal resistance and the entropy generation rate per unit length. The four-pass configuration with fully embedded tubing exhibited the highest exergetic performance, which means that the available work loss due to the combined effect of thermal resistance and pressure drop obtains a lower value in comparison to the other configurations.

Acknowledgments

The simulations were performed using the NTUA Cloud Computing infrastructure. The staff of the computer center is gratefully acknowledged for their technical support. The work was financially supported by the NTUA Special Account for Research.

REFERENCES

1. S. Vashisth, V. Kumar, K.D.P. Nigam, A Review on the Potential Applications of Curved Geometries in Process Industry, Ind. Eng. Chem. Res., vol. 47, pp. 3291-3337, 2008.
2. P. Naphon, S. Wongwises, A Review of Flow and Heat Transfer Characteristics in Curved Tubes, Ren. Sust. En. Rev., vol. 10, pp. 463-490, 2006.
3. H. Kobayashi, S. Lorente, R. Anderson, A. Bejan, Serpentine thermal coupling between a stream and a conducting body, J. Appl. Phys., vol. 111, 2012.
4. S.A. Berger, L. Talbot, L.S. Yao, Flow in Curved Pipes, Ann. Rev. Fluid Mech., vol.15, pp. 461-512, 1983.
5. S.V. Patankar, V.S. Pratap, D.B. Spalding, Prediction of Turbulent Flow in Curved Pipes, J. Fluid. Mech., vol. 67, pp. 583-595, 1975.
6. J.A. Fairbank, R.M.C. So, Upstream and Downstream Influence of pipe Curvature on the Flow through a Bend, Int. J. Heat Fluid Flow, vol. 8, pp. 211-217, 1987.
7. H. Sugiyama, D. Hitomi, Numerical Analysis of Developing Turbulent Flow in a 180^{o} Bend Tube by an Algebraic Reynolds Stress Model, Int. J. Numer. Meth. Fluids, vol 47, pp. 1431–1449, 2005.
8. S.C.R. Dennis., M. Ng, Dual Solutions for Steady Laminar Flow through a Curved Tube, Quart. J. Mech.Applied Math., vol. 35, pp. 305-324, 1982.
9. S. Yanase, N. Goto and K. Yamamoto, Dual Solutions of the Flow Through a Curved Tube, Fluid Dyn. Res., vol. 5, pp. 191-201, 1989.
10. I. Di Piazza, M. Ciofalo, Transition to Turbulence in Toroidal Pipes, J. Fluid Mech., vol. 687, pp. 72-117, 2011
11. K.C. Cheng, F.P. Yuen, Flow Visualization studies on Secondary Flow Patterns in Straight Tubes Downstream of a 180 deg Bend and in Isothermally Heated Horizontal Tubes, J. Heat Transfer, vol. 109, pp. 49-54, 1987.
12. D.E. Olson, B. Snyder, Upstream Scale of Flow Development in Curved Circular Pipes, J. Fluid. Mech., vol. 150, pp. 139-158, 1985.
13. M. Rowe, Measurements and Computations of Flow in Pipe Bends, J. Fluid. Mech., vol. 43, pp. 771-783, 1970.
14. J.H. Siggers, S.L. Waters, Steady Flows in Pipes with Finite Curvature, Phys. Fluids, vol. 17, pp. 077102 1-18, 2005.
15. Z.H. Yang, R.S. Ye, Symmetry-Breaking and Bifurcation Study on the Laminar Flows through Curved Pipes with a Circular Cross Section, J. Comp. Phys., vol. 127, pp. 73-87, 1996.

16. Y. Mori, W. Nakayama, Study on Forced Convective Heat Transfer in Curved Pipes (1st Report, Laminar Region), Int. J. Heat Mass Transfer, vol. 8, pp.67-82, 1965.
17. Y. Mori, W. Nakayama, Study on Forced Convective Heat Transfer in Curved Pipes (2nd Report, Turbulent Region), Int. J. Heat Mass Transfer, vol. 10, pp.37-59, 1967.
18. S. Jayanti, G.F. Hewitt, J.R. Knightley, Fluid Flow in Curved Cucts, Int. J. Num. Meth. Fluids vol. 10, pp. 253-266, 1990.
19. C.E. Kalb, J.D. Seader, Heat and Mass Transfer Phenomena for Viscous Flow in Curved Circular Tubes, Int. J. Heat Mass Transfer vol. 15, pp. 801-817, 1972.
20. J.M. Tarbell, M.R. Samuels, Momentum and Heat Transfer in Helical Coils, Chem. Eng. J., vol. 5, pp. 117-127, 1973.
21. M. Di Liberto, M. Ciofalo, A Study of Turbulent Heat Transfer in Curved Pipes by Numerical Simulation, Int. J. Heat Mass Transfer vol. 59, pp. 112-125, 2013.
22. M.M. Ohadi, E.M. Sparrow, Effect of a 180^{o} Bend on Heat Transfer in a Downstream Positioned Straight Tube, Int. J. Heat Mass Transfer vol. 33, pp. 1359-1362, 1990.
23. F. Bahiraei, R.K. Saray, A. Salezadeh, Investigation of Potential of Improvement of Helical Coils based on Avoidable and Unavoidable Exergy Destruction Concepts, Energy, vol. 36, pp.3113-3119, 2011.
24. Aavid Thermalloy, LLC, "High Contact Liquid Cold Plates" Datasheet, NH, USA.
25. I.K. Karathanassis, E. Papanicolaou, V. Belessiotis, G.C. Bergeles, Design and Optimization of a Micro Heat Sink for Concentrating/Photovoltaic Thermal (CPVT) Systems, Appl. Therm. Eng., vol. 59, pp 733-744, 2013.
26. F.R. Menter, Two-Equation Eddy-Viscosity Turbulence Models for Engineering Applications, AIAA J., vol. 32, pp. 1598–1605, 1994
27. ANSYS Inc., ANSYS CFX-Solver theory guide, Release 13.0, Canonsburg, PA 2010.
28. S. Yanase, K. Yamamoto, T. Yoshida, Effect of curvature on dual solutions of flow through a curved circular tube, Fluid Dyn. Res., vol. 13, pp. 217-228, 1994.
29. R.M.C. So, H.S. Zhang, Y.G. Lai, Secondary Cells and Separation in Developing Laminar Curved-Pipe Flows, Theoret. Comput. Fluid Dyn., vol. 3, pp. 141-162, 1991.
30. Y. Agrawal, L. Talbot, K. Gong, Laser anemometer study of flow development in curved circular pipes, J. Fluid. Mech. vol. 85, pp.497-518, 1978.
31. U.S. Choi, L. Talbot, I. Cornet, Experimental study of wall shear rates in the entry region of a curved tube, J. Fluid. Mech. vol. 93, pp. 465-489, 1979.
33. R.K. Shah, A.L. London Laminar Flow Forced Convection in Ducts: a Source Book for Compact Heat Exchangers, pp. 202-208, Academic press, New York, 1978.
34. D.W. Kim, Convection and flow boiling in microgaps and porous foam coolers, Ph.D. Thesis, University of Maryland, College Park, MD, 2007.
35. A. Bejan, Entropy Generation Minimization, 1^{st} ed., pp. 71-82, CRC Press, New York, 1996.

Tables

Table 1. Imposed boundary conditions (BC)

	Hydrodynamic BC	**Thermal BC**
Inlet	$w = w_i, u = 0, v = 0$	$T_f = T_i (= 298K)$
Outlet	$p_{ave} = 0$	$\frac{\partial^2 T_f}{\partial z^2} = 0$
Fluid-wall Interface	$u = v = w = 0$	-
Bottom surface	-	$-k_s \frac{\partial T_w}{\partial y} = q'' \left(= 28333\ W/m^2\right)$
Other outer surfaces	-	$-k_s \frac{\partial T_w}{\partial n} = 0$
Interface between successive domains	-	$T_w\big\|_{int} = T_f\big\|_{int}, -k_s \left.\frac{\partial T_w}{\partial n}\right\|_{int} = -k_f \left.\frac{\partial T_f}{\partial n}\right\|_{int}$

Table 2. Grid independence study

Grid	**Coarse**	**Intermediate**	**Fine**
Elements	$1.24 \cdot 10^6$	$2.61 \cdot 10^6$	$4.06 \cdot 10^6$
Pressure drop [Pa]	1804.75	1835.50	1847.05
T_{max} [K]	309.68	309.62	309.60
Nu [-]	50.12	50.88	51.35

Table 3. Comparative results for the different cooling configuration.

	two-pass (PE)	**two-pass (FE)**	**four-pass (PE)**	**four-pass (FE)**
R_{th} [K/W]	0.0232	0.0196	0.0158	0.0140
ΔP [Pa]	859.56	859.56	1835.48	1835.48
StDev T [K]	0.524	0.678	0.761	0.925
PI [-]	4490.41	4605.00	4378.32	4614.42
$\dot{S}'_{gen}$ [W/mK]	0.0808	0.0788	0.0219	0.0209
Be	0.966	0.965	0.865	0.858

Figure Captions

Figure 1. Geometrical layout of the cooling configurations: (a) two-pass, (b) four-pass.

Figure 2. Computational grid: (a) detail view of the bends area and (b) sectional view.

Figure 3. (a) Comparison of the fully developed velocity profiles calculated in the present study against those available in Ref. **[5]** for turbulent flow at Re=25000. (b-e) Comparison of the numerically calculated horizontal velocity profiles against the experimental results of Ref. **[6]** for laminar flow at Re=400: (b), (c) s/2R=0.5 and (d), (e) s/2R=5.0.

Figure 4. Non-dimensional axial velocity profiles at the tube horizontal symmetry plane downstream of the bend: (a) two-pass and (b) four-pass configuration. Three dimensional streamlines at the area of the bends: (c) two-pass and (d) four-pass configuration.

Figure 5. Wall shear stress distribution at the wall on the tube horizontal symmetry plane: (a) two-pass and (b) four-pass configuration.

Figure 6 Contour plots of the vorticity projection normal to cross-stream planes in the curved and straight downstream section: (a) two-pass configuration, (b) four-pass configuration. (c) Cross-sectional averaged value of the total vorticity magnitude in the tube curved section.

Figure 7. Contour plots of the turbulent kinetic energy in the tube cross section: (a) two-pass configuration, (b) four-pass configuration. (c) Distribution of the average turbulent kinetic energy as a function of the unwound coordinate S^*. ($S_0^* = 60.50$).

Figure 8. Secondary-flow patterns at a cross-stream plane ($\varphi=90^o$) as a function of the Reynolds number (two-pass configuration).

Figure 9. Two-pass configuration: (a) Cross-sectional averaged values of the vorticity magnitude at the tube curved section, (b) maximum vorticity magnitude of the distinct vortical structures at a sample plane ($\varphi=90^o$) vs. the Reynolds number.

Figure 10. Two-pass configuration: distribution of the average turbulent kinetic energy on cross-stream planes as a function of the unwound coordinate S^* ($S_0^* = 60.50$).

Figure 11. Temperature contour plots in the fluid region (solid top surface shown at $Y^*=1$): (a) upstream tube section of the two-pass configuration, (b) downstream tube section of the two-pass configuration, (c) downstream tube section of the four-pass configuration (second passage), (d) at the passages of the four-pass configuration.

Figure 12. Temperature contour plots at various heights within the substrate area of the heat sink: (a) two-pass and (b) four-pass configuration.

Figure 13. Vertical temperature profiles at the heat sink streamwise mid-length (Z*=30.25): (a) two-pass and (b) four-pass configuration.

Figure 14. Local Nusselt distribution: (a) two-pass configuration, (b) four-pass configuration, first and third passage (c) four-pass configuration, second and fourth passage.

Figures

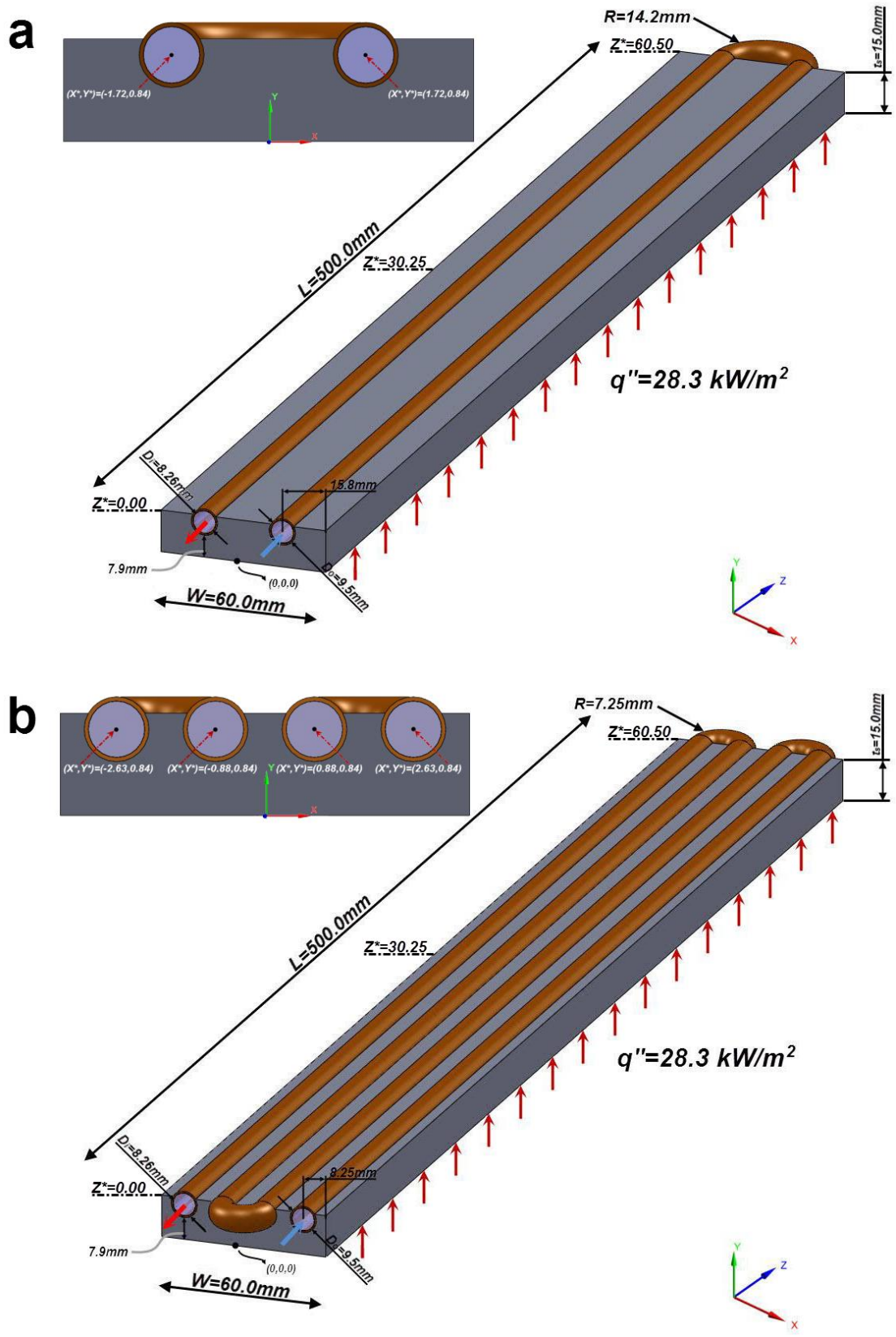

Figure 1. Geometrical layout of the cooling configurations: (a) two-pass, (b) four-pass.

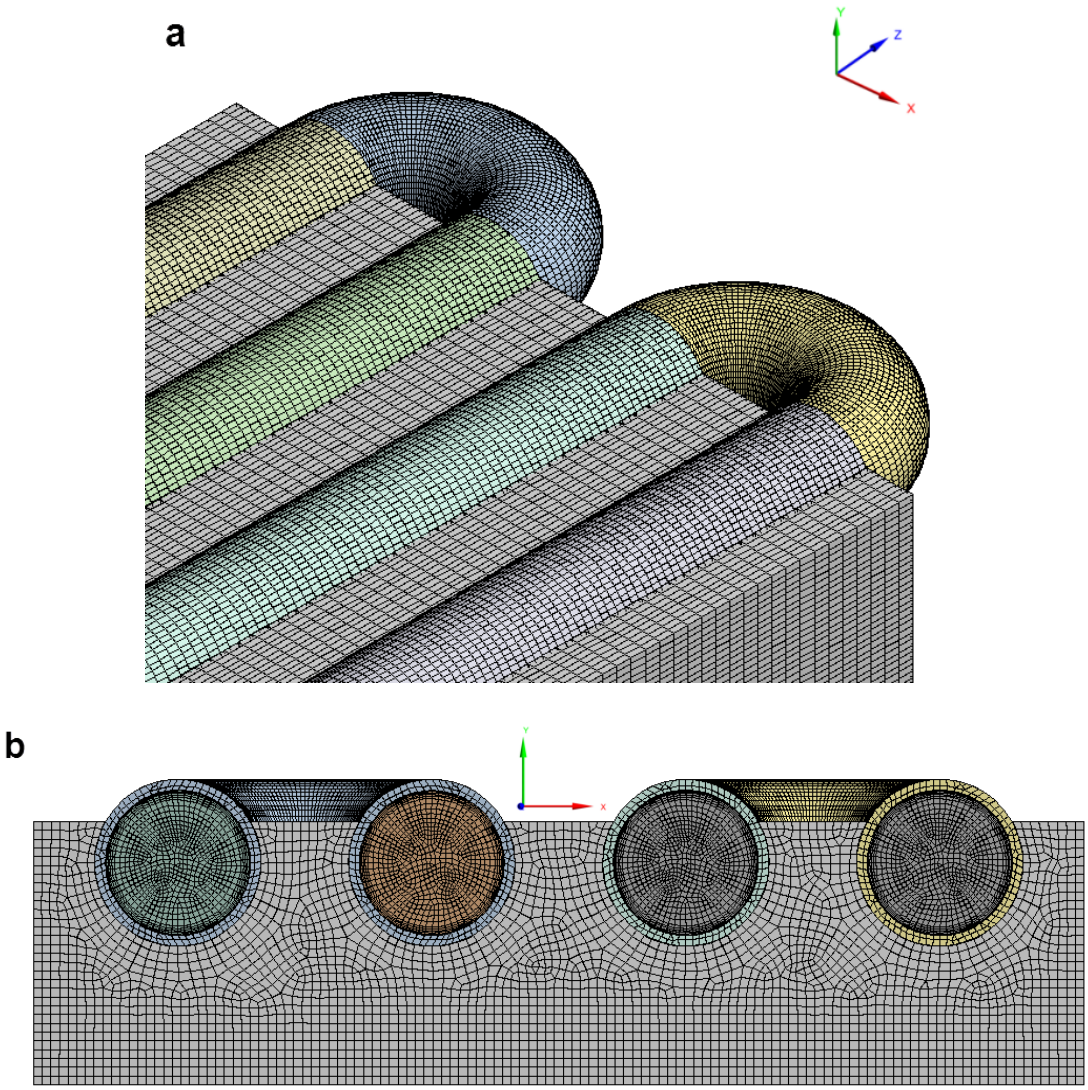

Figure 2. Computational grid: (a) detail view of the bends area and (b) sectional view.

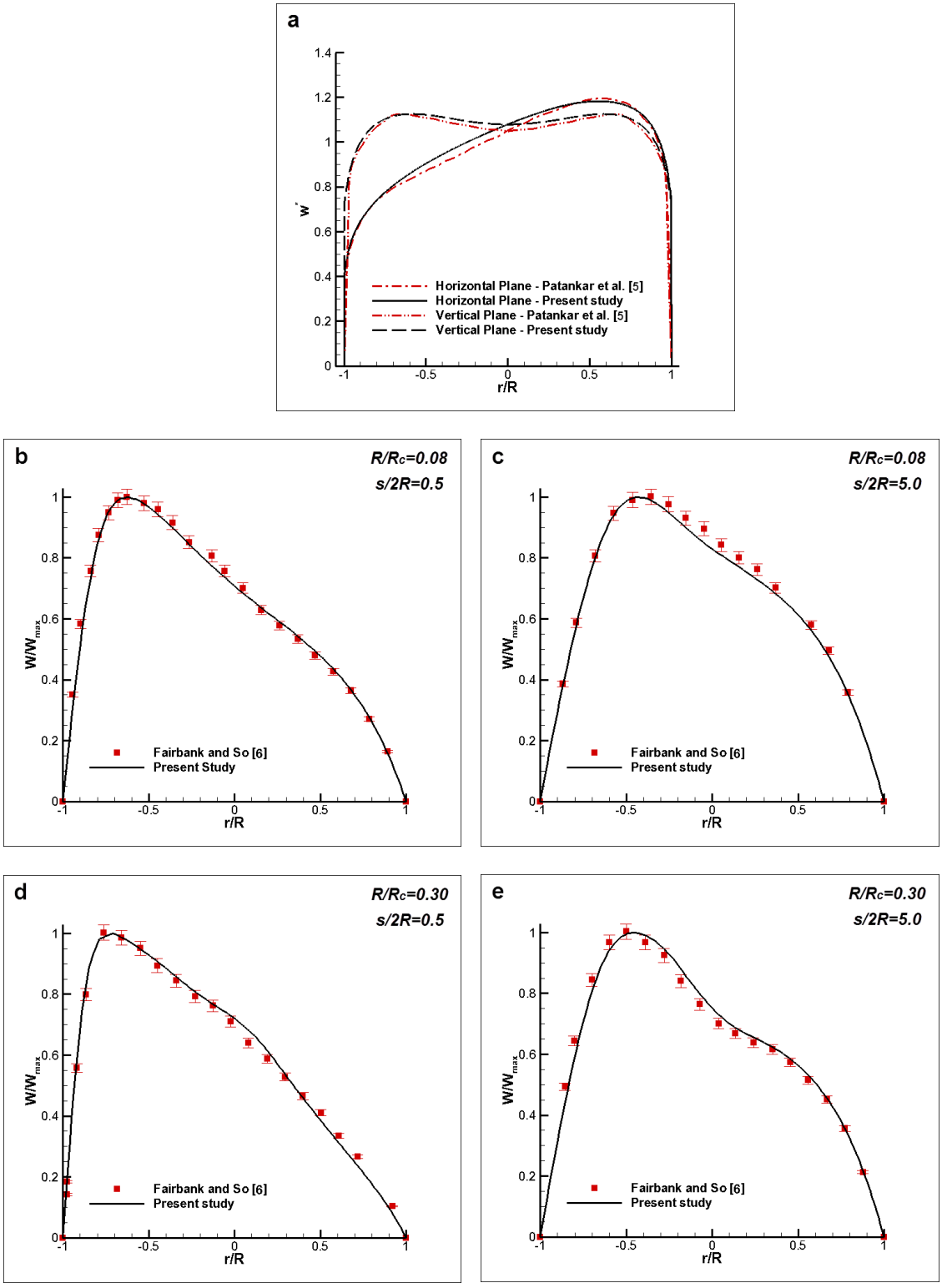

Figure 3. (a) Comparison of the fully developed velocity profiles calculated in the present study against those available in Ref. **[5]** for turbulent flow at Re=25000. (b-e) Comparison of the numerically calculated horizontal velocity profiles against the experimental results of Ref. **[6]** for laminar flow at Re=400: (b), (c) s/2R=0.5 and (d), (e) s/2R=5.0.

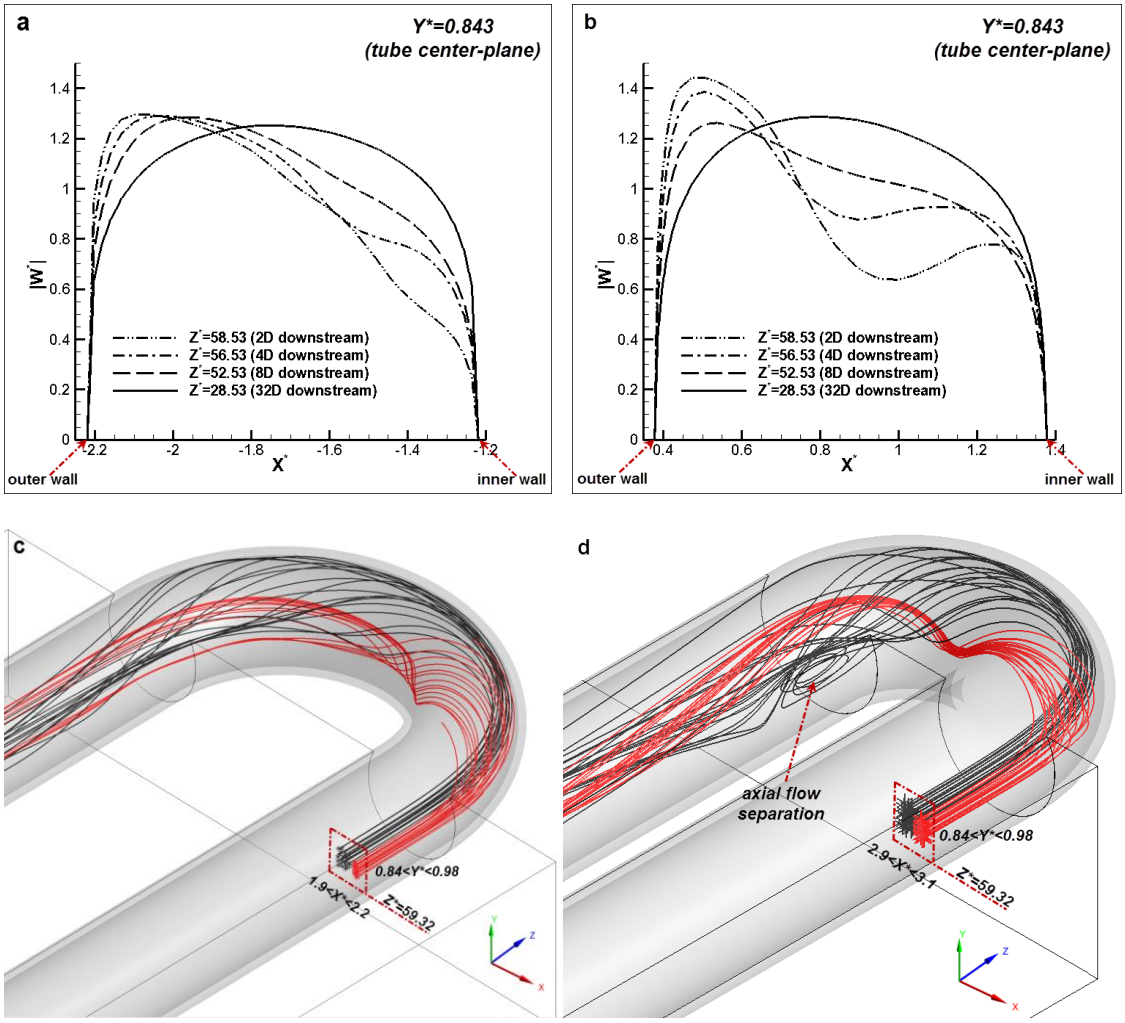

Figure 4. Non-dimensional axial velocity profiles at the tube horizontal symmetry plane downstream of the bend: (a) two-pass and (b) four-pass configuration. Three dimensional streamlines at the area of the bends: (c) two-pass and (d) four-pass configuration.

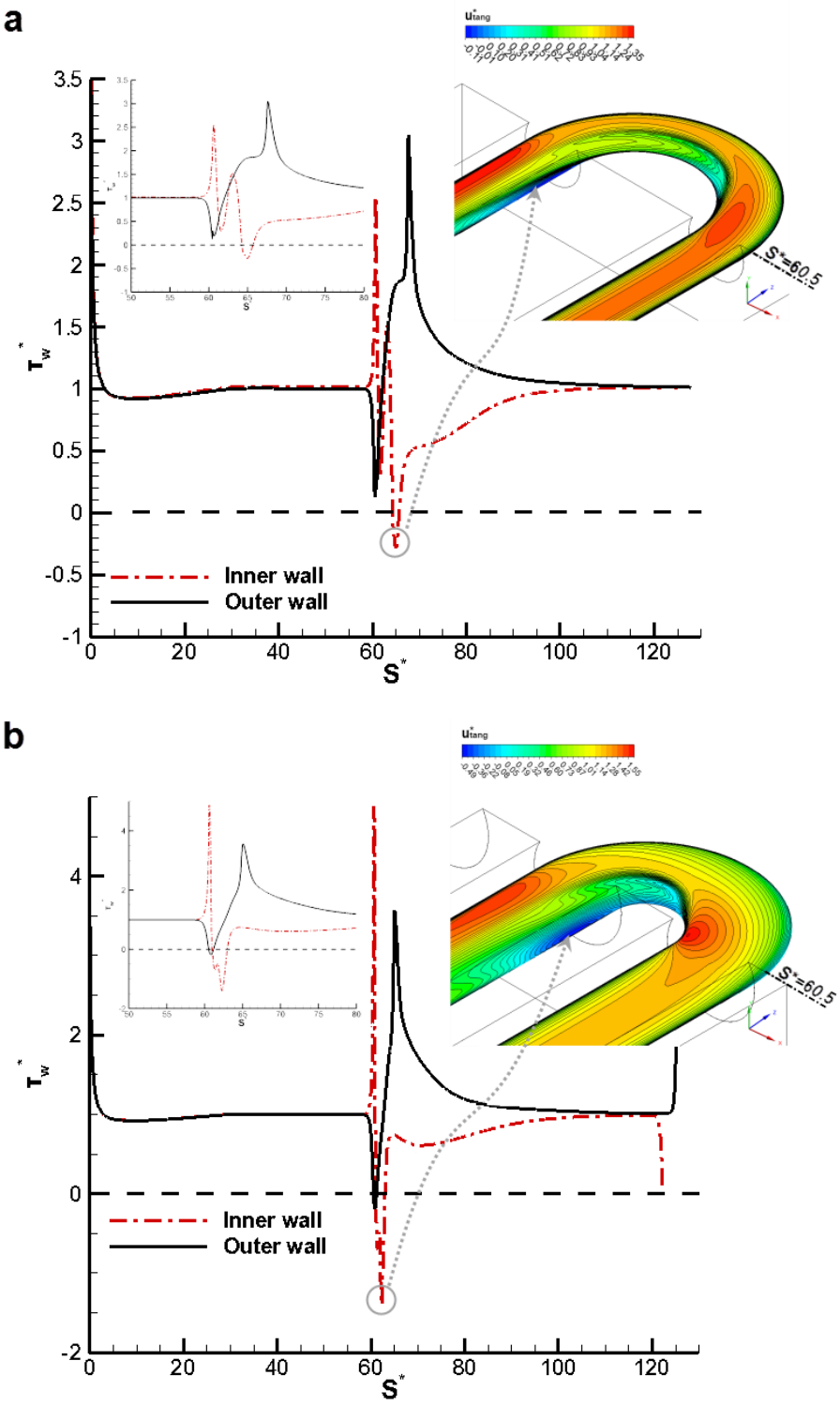

Figure 5. Wall shear stress distribution at the wall on the tube horizontal symmetry plane: (a) two-pass and (b) four-pass configuration.

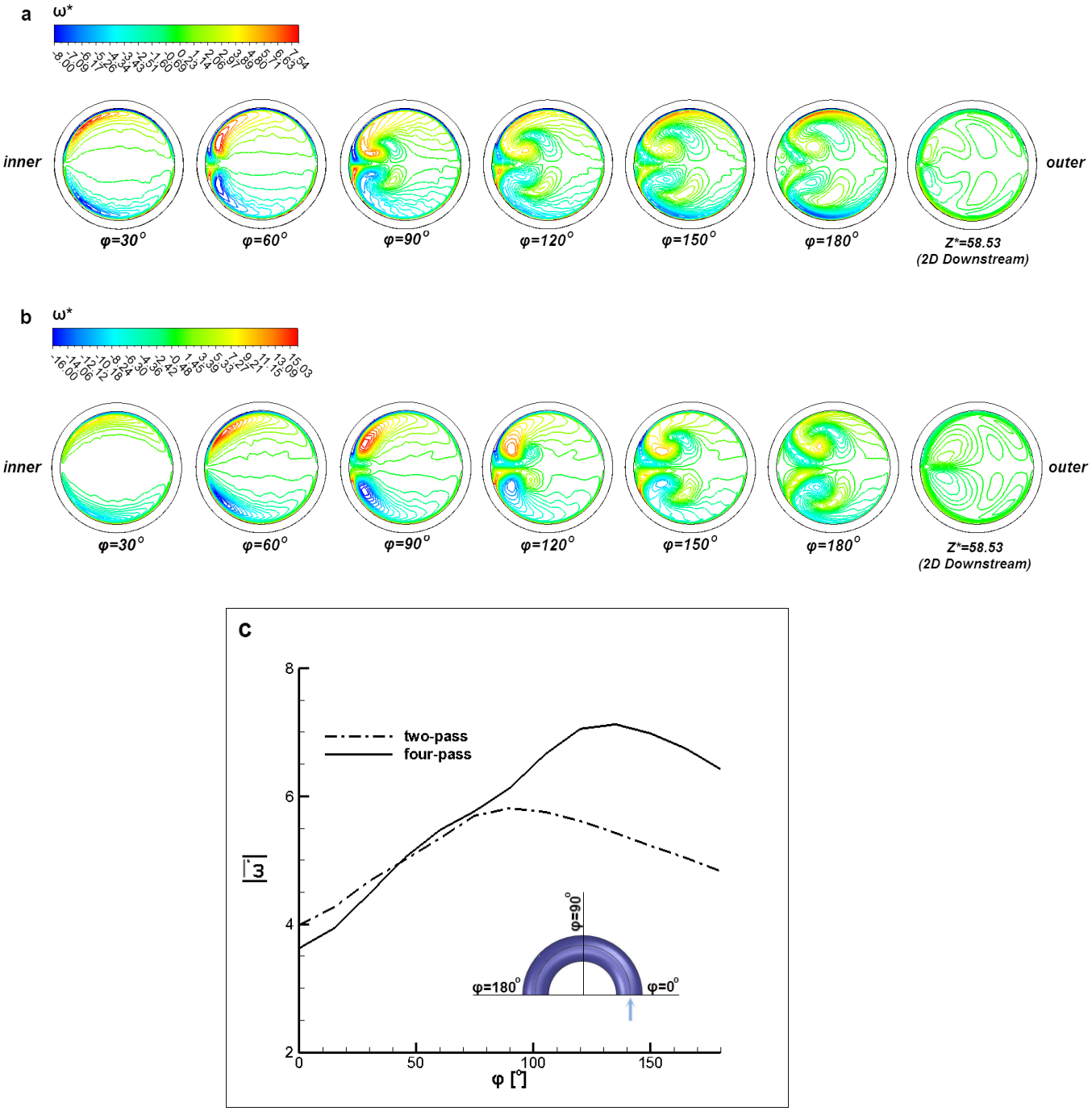

Figure 6. Contour plots of the vorticity projection normal to cross-stream planes in the curved and straight downstream section: (a) two-pass configuration, (b) four-pass configuration. (c) Cross-sectional averaged value of the total vorticity magnitude in the tube curved section

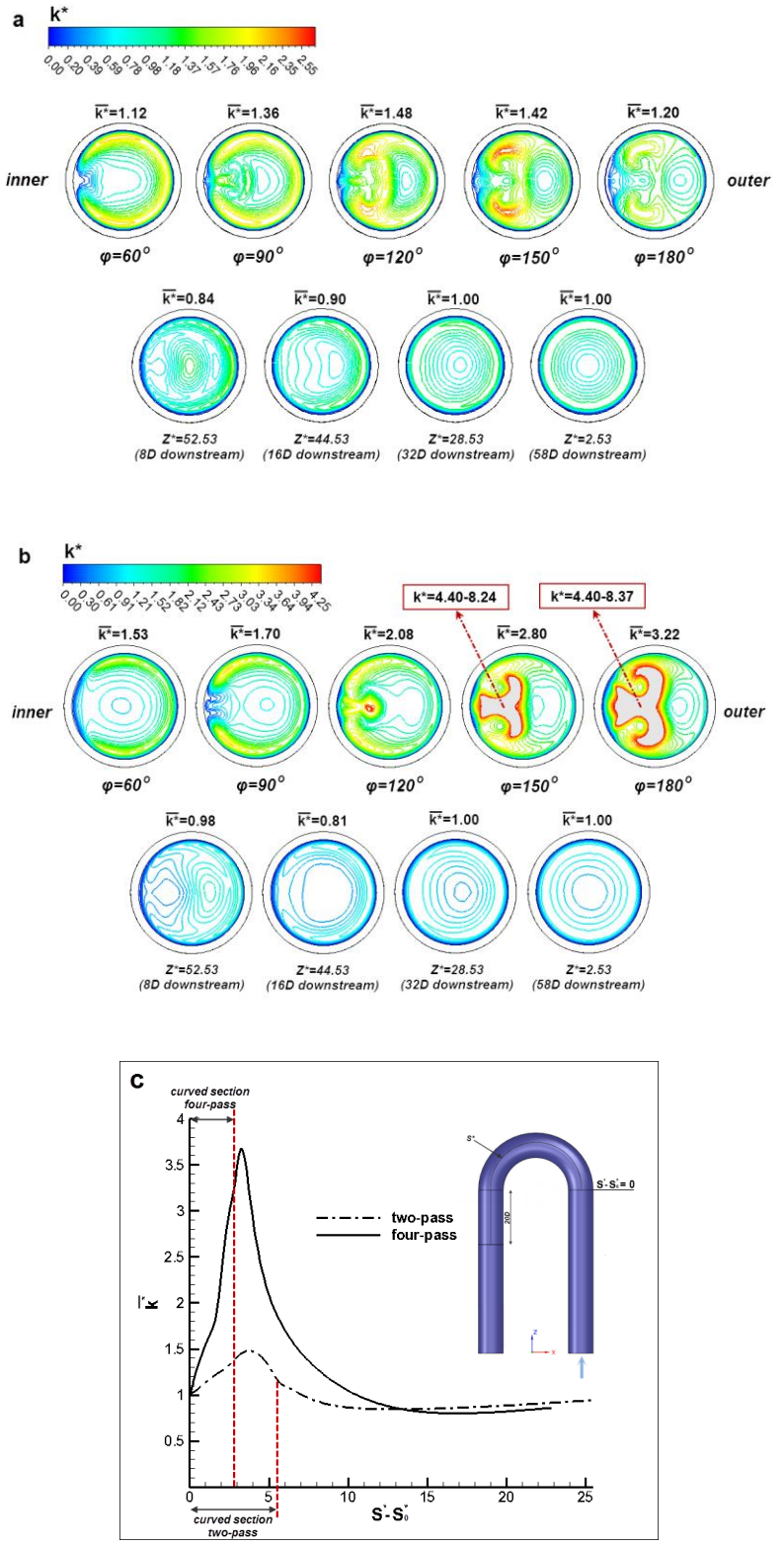

Figure 7. Contour plots of the turbulent kinetic energy in the tube cross section: (a) two-pass configuration, (b) four-pass configuration. (c) Distribution of the average turbulent kinetic energy as a function of the unwound coordinate S^* ($S_0^* = 60.50$).

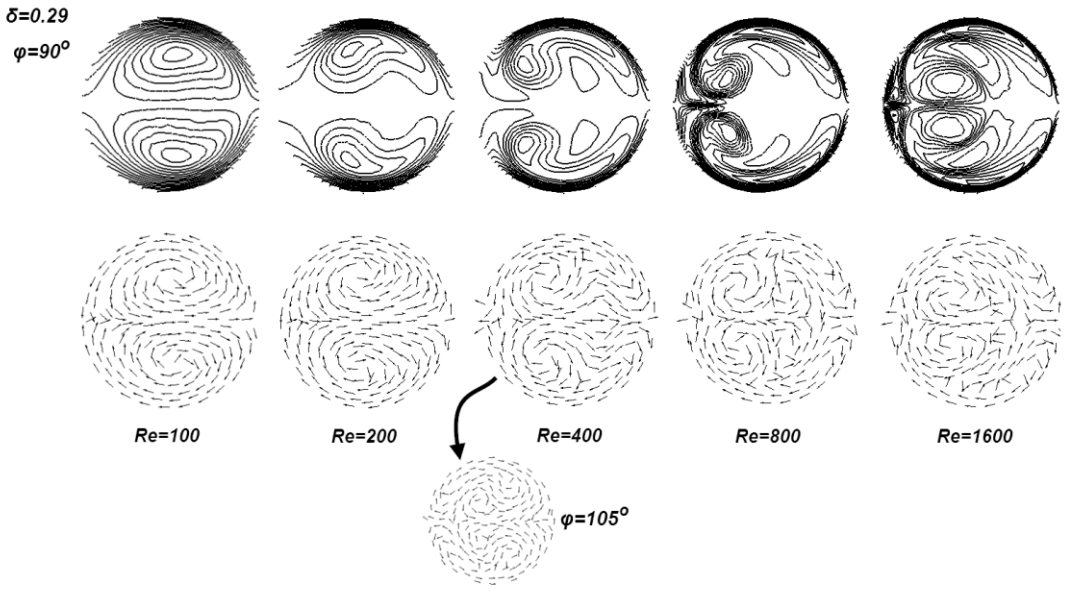

Figure 8. Secondary-flow patterns at a cross-stream plane ($\varphi=90^{o}$) as a function of the Reynolds number (two-pass configuration).

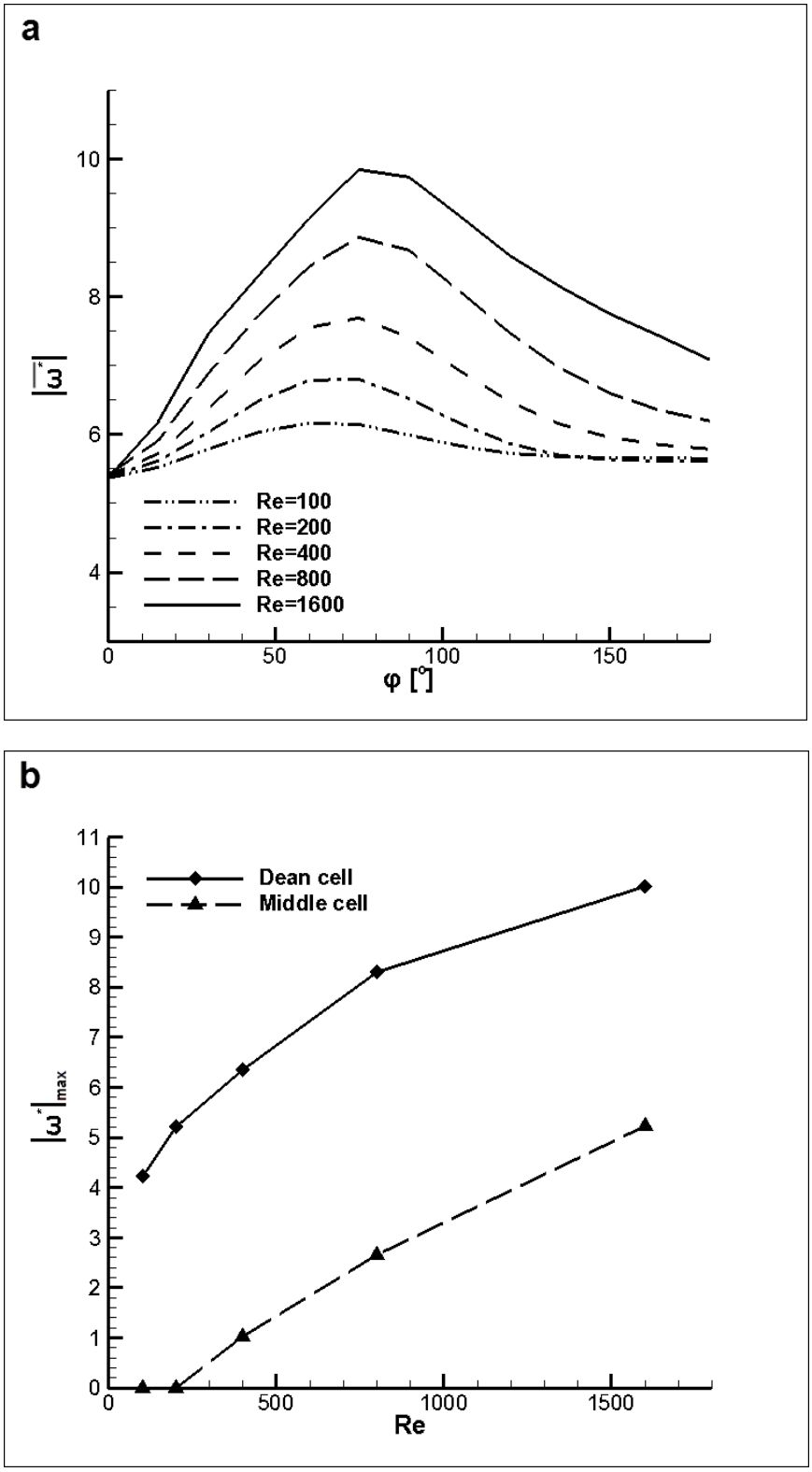

Figure 9. Two-pass configuration: (a) Cross-sectional averaged values of the vorticity magnitude at the tube curved section for various Reynolds numbers values, (b) maximum vorticity magnitude of the distinct vortical structures at a sample plane ($\varphi=90^{o}$) vs. the Reynolds number.

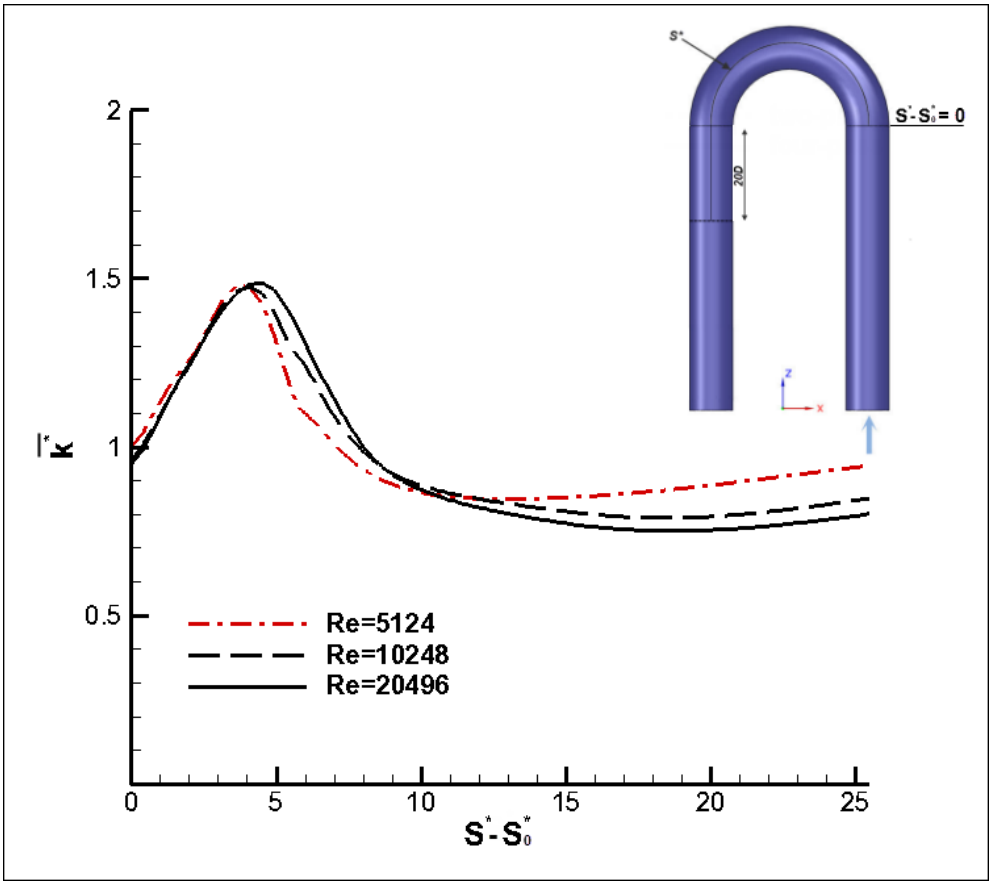

Figure 10. Two-pass configuration: distribution of the average turbulent kinetic energy on cross-stream planes as a function of the unwound coordinate S^* ($S_0^* = 60.50$).

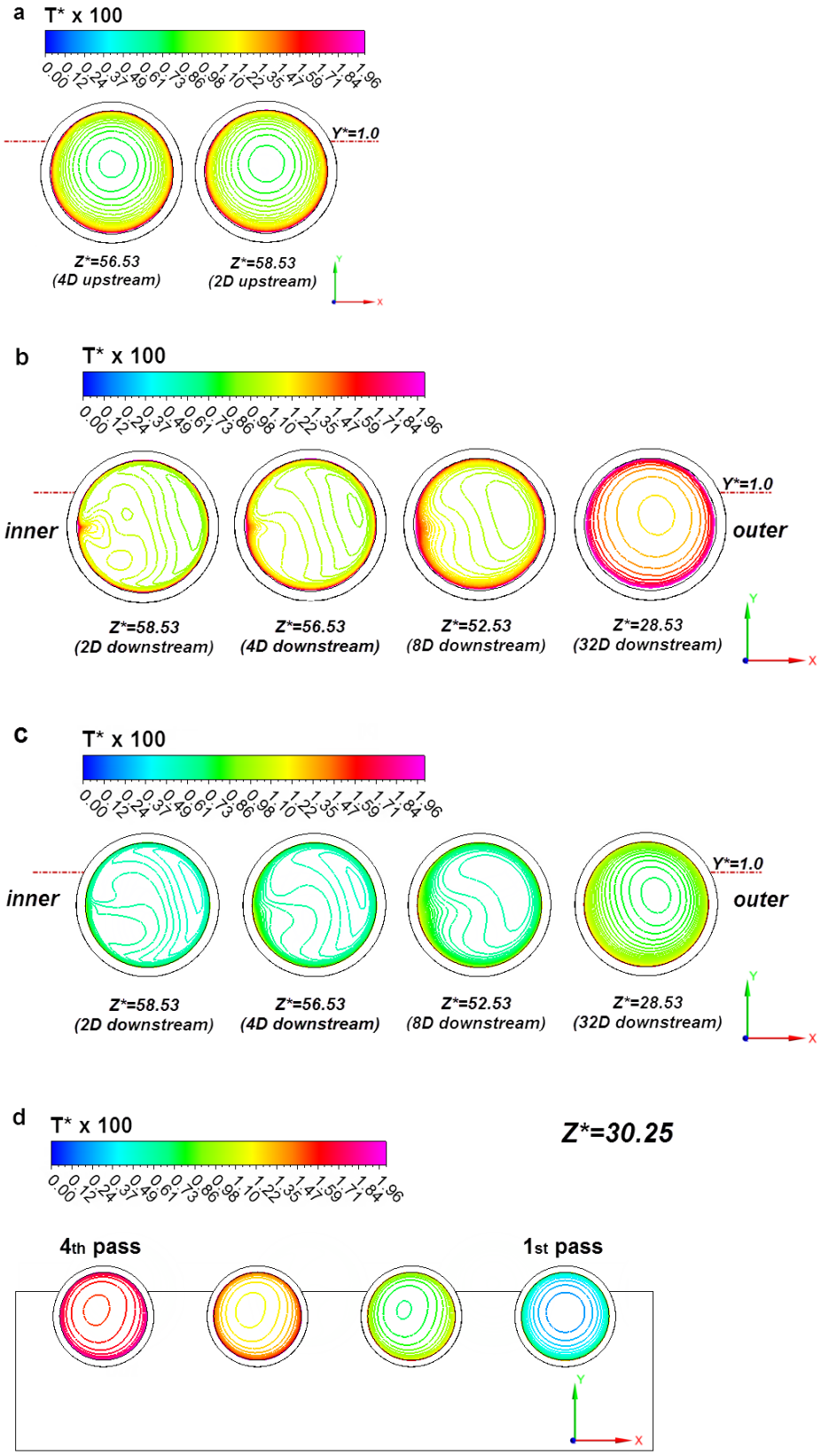

Figure 11. Temperature contour plots in the fluid region (solid top surface shown at $Y^*=1$): (a) upstream tube section of the two-pass configuration, (b) downstream tube section of the two-pass configuration, (c) downstream tube section of the four-pass configuration (second passage), (d) at the passages of the four-pass configuration.

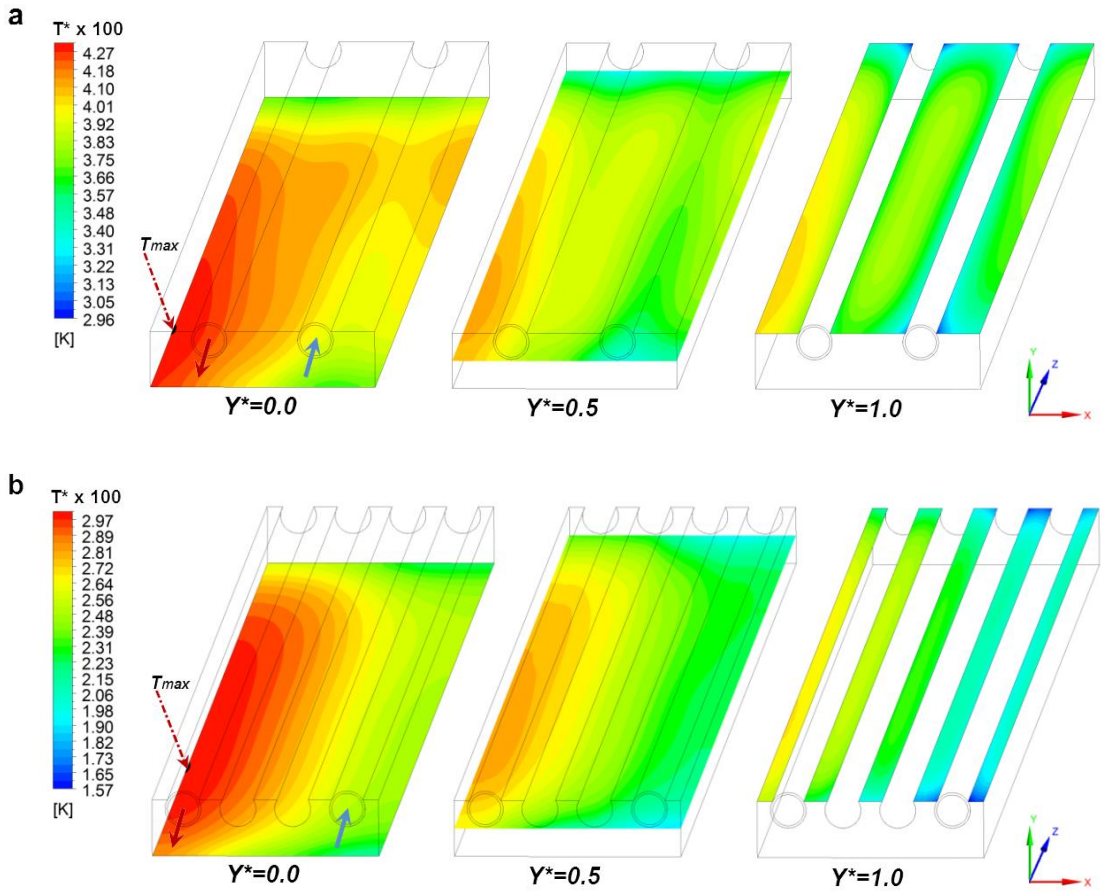

Figure 12. Temperature contour plots at various heights within the substrate area of the heat sink: (a) two-pass and (b) four-pass configuration.

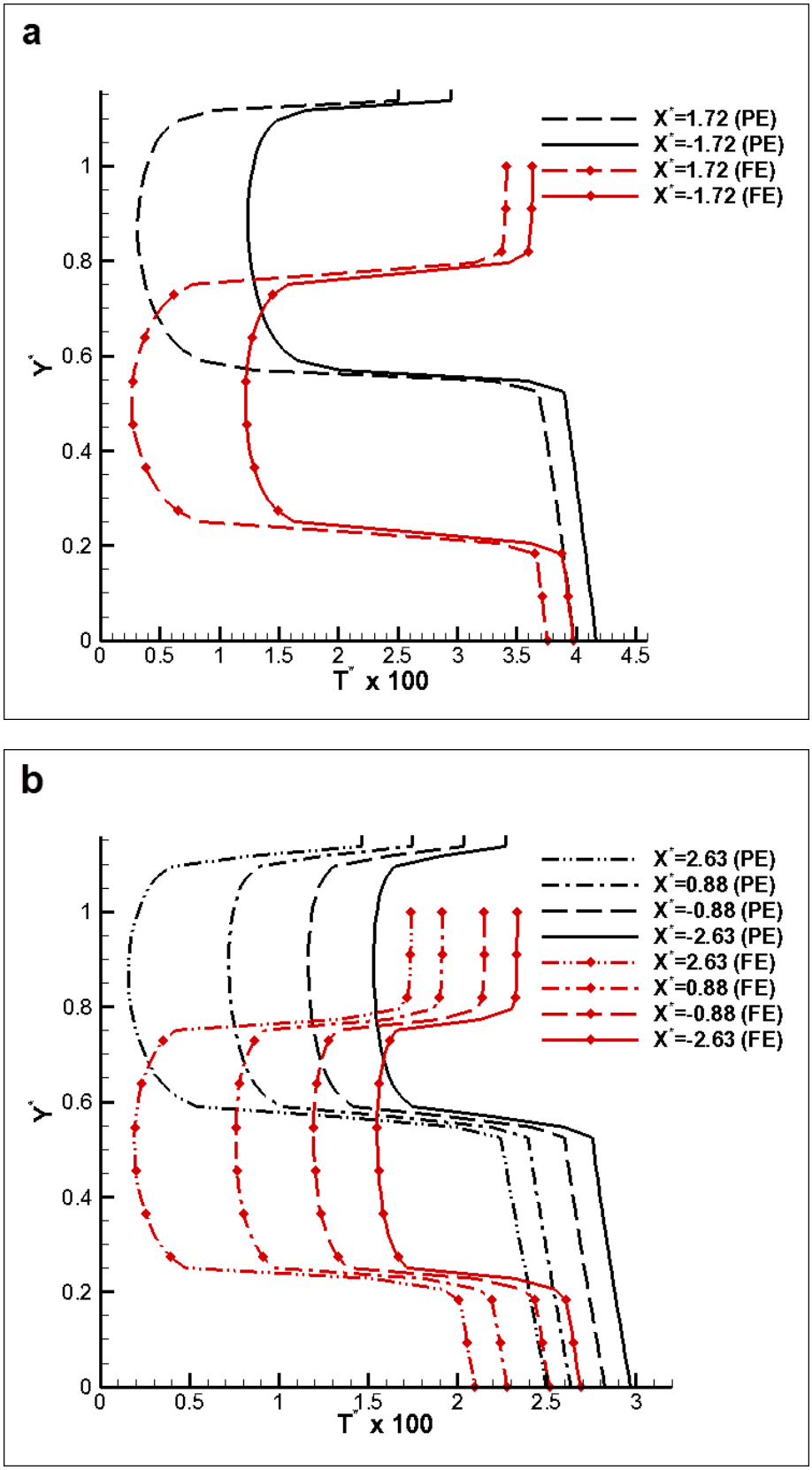

Figure 13. Vertical temperature profiles at the heat sink streamwise mid-length (Z*=30.25): (a) two-pass and (b) four-pass configuration.

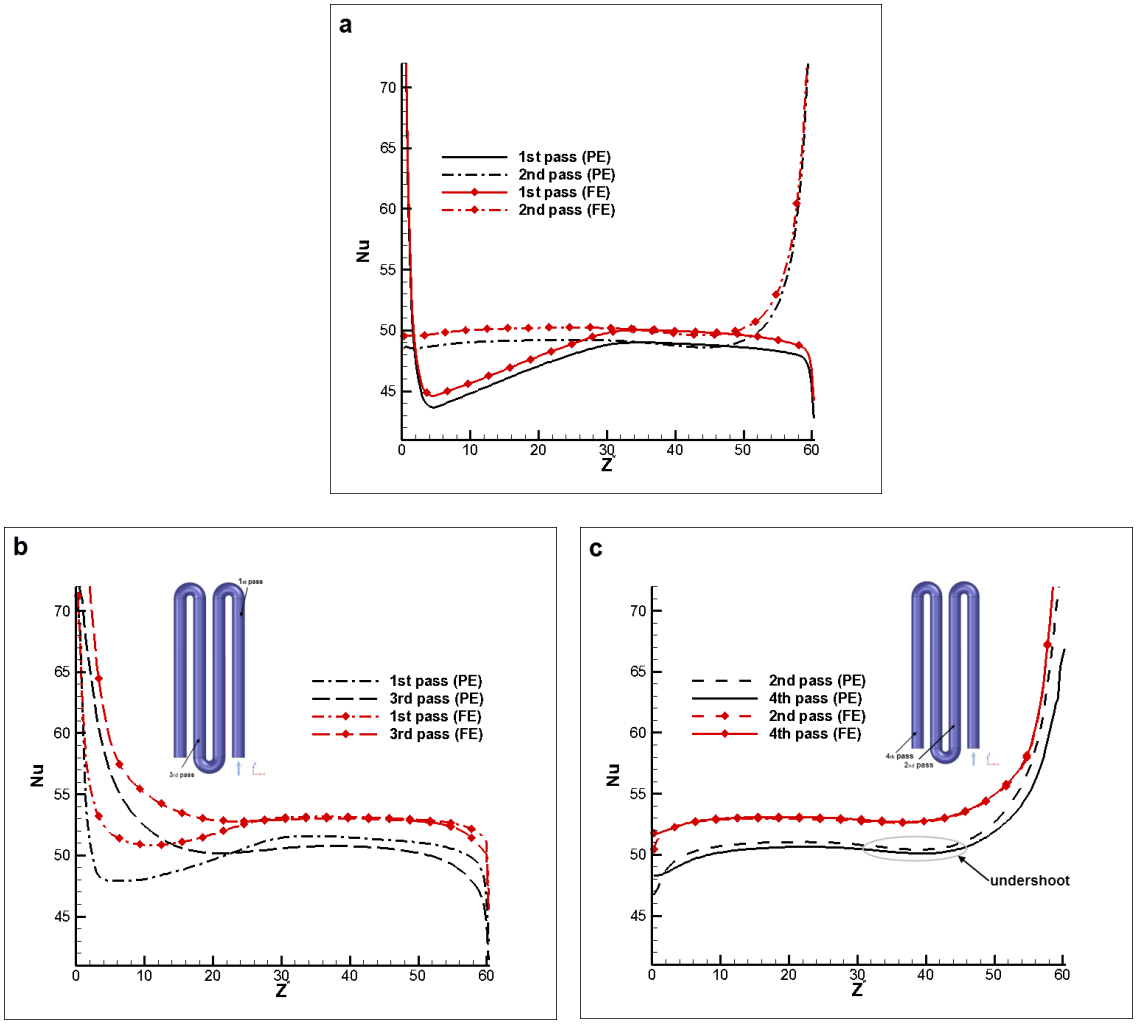

Figure 14. Local Nusselt distribution in the substrate area: (a) two-pass configuration, (b) four-pass configuration, first and third passage (c) four-pass configuration, second and fourth passage.